Spring 2019

# Site-Directed Spin Label EPR Studies of the Interaction Between the Influenza A Proteins (M1 and M2) Involved in Viral Assembly

Abigail J. Wong-Rolle , '19

## Recommended Citation

Wong-Rolle, Abigail J. , '19, "Site-Directed Spin Label EPR Studies of the Interaction Between the Influenza A Proteins (M1 and M2) Involved in Viral Assembly" (2019). *Senior Theses, Projects, and Awards*. 243.
https://works.swarthmore.edu/theses/243

# Site-Directed Spin Label EPR Studies of the Interaction Between the Influenza A Proteins (M1 and M2) Involved in Viral Assembly

Presented as a Senior Honors Thesis in Chemistry

**Abigail Wong-Rolle**
Department of Chemistry and Biochemistry
Swarthmore College
April 15, 2019
**Advisor: Kathleen P. Howard, PhD**

# Table of Contents

# List of Figures and Tables

# List of Common Abbreviations

AEBSF - 4-(2-aminoethyl)benzenesulfonyl fluoride hydrochloride

BLI – biolayer interferometry

BME – β-mercaptoethanol

CW – continuous wave

DLS – dynamic light scattering

EDTA – ethylenediamine-*N,N,N',N'*-tetraacetic acid

EPR – electron paramagnetic resonance

GuHCl – guanidinium chloride

HA – hemagglutinin

$\text{His}_6$ tag – six histidine tag

IPTG – isopropyl β-D-1-thiogalactopyranoside

LB broth – Luria broth

M1 – matrix protein 1 from influenza A

M2 – matrix protein 2 from influenza A

M2FL – full-length M2 protein

MTSL – (1-oxyl-2,2,5,5-tetramethyl-Δ3-pyrroline-3-methyl)-methanethiosulfonate spin label

NA – neuraminidase

NEP – nuclear export protein

NiEDDA – ni(II)ethylenediaminediacetic acid

OD – optical density

OG – octyl β-D-glucopyranoside

PDB – Protein Data Bank

PHE – 4-[3-(4-acetyl-3-hydroxy-2-propylphenoxy)-propoxy]phenoxyacetic acid

POPC – 1-palmitoyl-2-oleoyl-*sn*-glycero-3-phosphocholine

POPG – 1-palmitoyl-2-oleoyl-*sn*-glycero-3-[phosphor-*rac*-(1glycerol)]

SDS-PAGE – sodium dodecyl sulfate–polyacrylamide gel electrophoresis

SDSL – site-directed spin-labeling

SMALPS – styrene maleic anhydride co-polymer lipid particles

SPR – surface plasmon resonance

TCEP – tris(2-carboxyethyl)phosphine

Tris – tris(hydroxymethyl)aminomethane

TM – transmembrane

VLPs – virus-like particles

vRNP – complex consisting of viral RNA wrapped around protein

WT – wild-type

## Abstract

Influenza A presents a significant concern for public health as it is the cause of seasonal outbreaks and global pandemics. The influenza A proteins, matrix protein 1 (M1) and matrix protein 2 (M2), have been shown to be essential for the propagation of new viruses, especially through their roles in viral assembly and budding. The M2 cytoplasmic tail interacts with the M1 protein, recruiting it to the viral budding site and enabling proper packaging of the viral genome. The Howard lab has previously characterized residues 50-70 in the M2 cytoplasmic tail and the M2 protein's conformational equilibria by site-directed spin label electron paramagnetic resonance (SDSL-EPR). This work lays groundwork for the establishment of a system in which to see changes in the M2 protein upon M1 binding. Methods for the overexpression and purification of the M1 protein are presented. Selected M2 sites (43, 57, 68) were studied by SDSL-EPR in the presence of N-terminal M1 (residues 1-165), with M2 sites 43 and 57 acting as indicators of the M2 protein's conformational dynamics. Binding between M1 and M2 could not be rigorously established, but preliminary results suggest little change in the M2 protein in the presence of the M1 protein.

# Chapter 1 : Introduction

## *1.1. Influenza A: A Public Health Concern*

The influenza virus has been the cause of global pandemics and presents a considerable threat for possible future pandemics. The largest influenza pandemic in known history was the 1918 Spanish flu outbreak which swept Europe at the end of World War I.[1] This pandemic infected about 500 million people and killed over 50 million people worldwide. More lives were lost to influenza than the war, which resulted in the loss of about 18 million lives.[2] The particular strain of influenza virus that caused the Spanish flu likely originated in Asia and was a form of influenza A. There are four overarching types of influenza virus: A, B, C, and D. Influenza A and B are responsible for the strains that have caused pandemics and the seasonal flu. Influenza A, however, causes the most deadly pandemics and the most severe cases of flu.[1,2]

Approximately 3 to 5 million cases of severe illness are caused by annual influenza outbreaks.[2] During the 2018 flu season, 34 million Americans got the flu, with 710,000 people hospitalized and 56,000 fatalities.[3] The flu vaccine, which is formulated each year to match up with the particular strains of influenza that are predicted, was only about 36% effective in 2018.[2] When vaccinations fail or those affected are very young, very old, or immune-compromised, antivirals allow for the treatment of the flu after infection. Currently, the Centers for Disease Control and Prevention recommends four antivirals for use in treating influenza A and B: oseltamivir (Tamiflu), zanamivir (Relenza), peramivir (Rapivab), and baloxavir (Xofluza).[2,4] All of these antivirals, except baloxavir (which targets a subunit of the viral polymerase), target the same protein in influenza: neuraminidase (NA).[4] Reliance on only a few antivirals, especially antivirals that target the same protein could lead to the development of drug resistant viruses. A greater, atomic level of understanding of the influenza viral life cycle could yield potential antiviral targets.

### *1.2. Influenza A Viral Life Cycle*

The influenza A virus is a pleomorphic enveloped virus, commonly exhibiting filamentous or spherical morphology. Influenza is classified as an orthomyxovirus and has eight segments of negative-sense, single stranded RNA that encode for viral proteins: polymerase proteins that make up the viral RNA polymerase complex, a nucleoprotein, two surface glycoproteins, two matrix proteins, and non-structural proteins.[1,5,6] A cartoon representation of the influenza A virus is pictured in Figure 1.1A.

The influenza A viral life cycle is illustrated in Figure 1.1B and begins with the entry of a virus into a host cell. This process begins when one of the two surface glycoproteins, hemagglutinin (HA), attaches the virus to sialic acid receptors on the host cell surface.[7] The virus is then endocytosed into the host cell. The low pH of the endosome induces conformational change in HA that leads to membrane fusion of viral envelope and endosome. The matrix protein 2 (M2) undergoes a conformational change, leading to the opening of its ion channel, acidifying the virus interior. At neutral pH, within the virus, matrix protein 1 (M1) forms a membrane-associated layer that protects and stabilizes the viral genome. The viral genome forms a complex known as vRNP, which is made up of viral RNA around nucleoprotein (NP) and a small quantity of nuclear export protein (NEP), with the three polymerase proteins that make up the RNA polymerase complex at one end. M1 holds the vRNP complexes close to the membrane.[5,7]

Acidification of the virus interior leads to a conformational change in M1, which releases vRNP. The vRNP enters the nucleus and negative sense RNA is converted to positive sense RNA by the viral RNA polymerase complex. The virus utilizes the host cell's transcription machinery to reproduce its genome and produce more viral proteins. New vRNPs are formed and exported from the host cell nucleus. The three viral membrane proteins (HA, NA, and M2) cluster on the surface of the host cell. M2 is proposed to recruit M1 associated with vRNP to the membrane at the budozone site. A new viral particle buds off from the host cell, with final membrane scission facilitated by M2.[8–10] NA cleaves sialic acid from glycoproteins and glycolipids of the host cell preventing viral re-entry.[5,7,11]

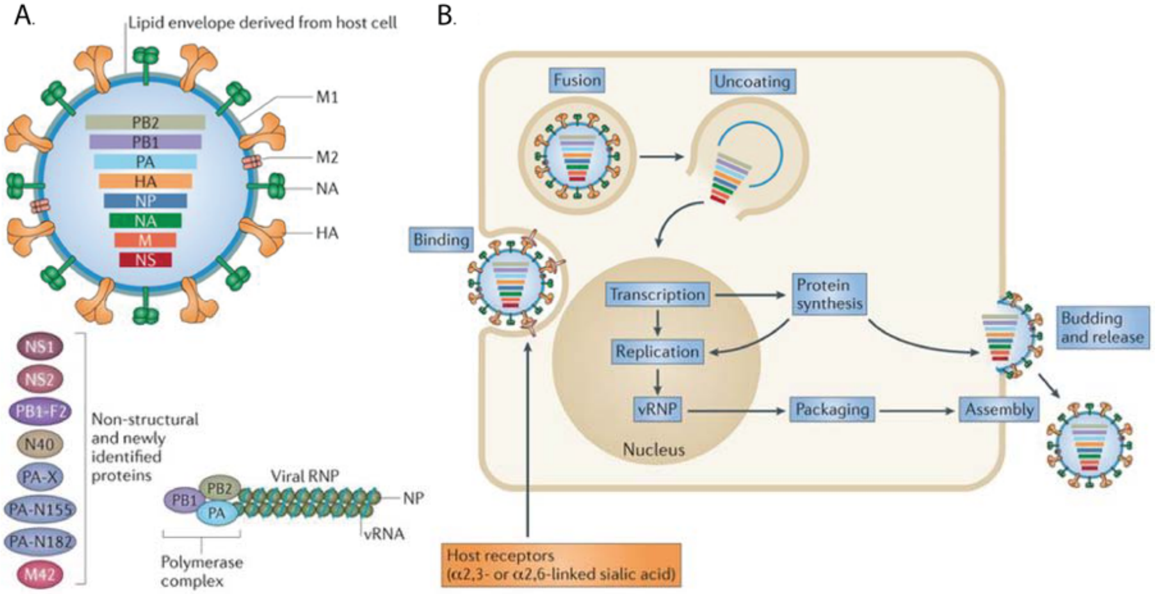

**Figure 1.1. Influenza A and the viral life cycle.** (A) The influenza A virus is an enveloped virus which consists of eight segments of RNA that encode for viral proteins: polymerase proteins that make up the viral RNA polymerase complex, a nucleoprotein, two surface glycoproteins, two matrix proteins, and non-structural proteins. Polymerase proteins, nucleoprotein and viral RNA form the vRNP complex. (B) The viral life cycle begins with viral entry into a host cell. HA binds to sialic acid and the virus is endocytosed into host cell. Low pH causes M2 pore to open and acidify virus interior. M1 dissociates from vRNP, matrix layer dissolves and HA mediates membrane fusion. Viral genome is transcribed and replicated. M1 binds to vRNP. M1 and NEP facilitate genome nuclear export. Surface proteins cluster on lipid raft and direct M1-vRNP. M1 forms matrix layer, elongating virion. New virus particle buds off from host cell. From[6]

### *1.3. The Matrix Protein 2*

M2 is a 97 residue membrane protein that consists of an N-terminal domain (1-21), a transmembrane (TM) helix domain (22-46), a membrane-proximal amphipathic α-helix (AH) region and a cytoplasmic tail (Fig. 1.2A). M2 forms a homotetramer, allowing it to serve as a proton channel. The transmembrane helix domain, which forms this channel, has been extensively studied, as it plays an important role in viral uncoating. The structure of the M2 protein has been elucidated using multiple techniques including solid state NMR,[12] solution NMR,[13] X-ray crystallography,[14–16] and electron paramagnetic resonance (EPR).[17] Published structures show different arrangements for the cytoplasmic region of the M2 protein, as the protein can adopt multiple conformations (Fig. 1.2B).[18] The Howard lab has focused on characterizing the structure of this relatively less studied region which has a role in viral budding and genome packaging.[8,9,19]

Previous reports from the Howard lab have studied the multiple conformational sub-states of the M2 protein in different pH and membrane environments.[17,20] The Howard lab has also collected information on site by site mobility and membrane depth for M2 residues 50-70 in a 4:1 1-palmitoyl-2-oleoyl-*sn*-glycero-3-phosphocholine:1-palmitoyl-2-oleoyl-*sn*-glycero-3-[phosphor-*rac*-(1glycerol)] (POPC:POPG) bilayer environment.[21,22] The intent of present and future work is to expand the characterization of the M2 cytoplasmic tail to include its interaction with the M1 protein.

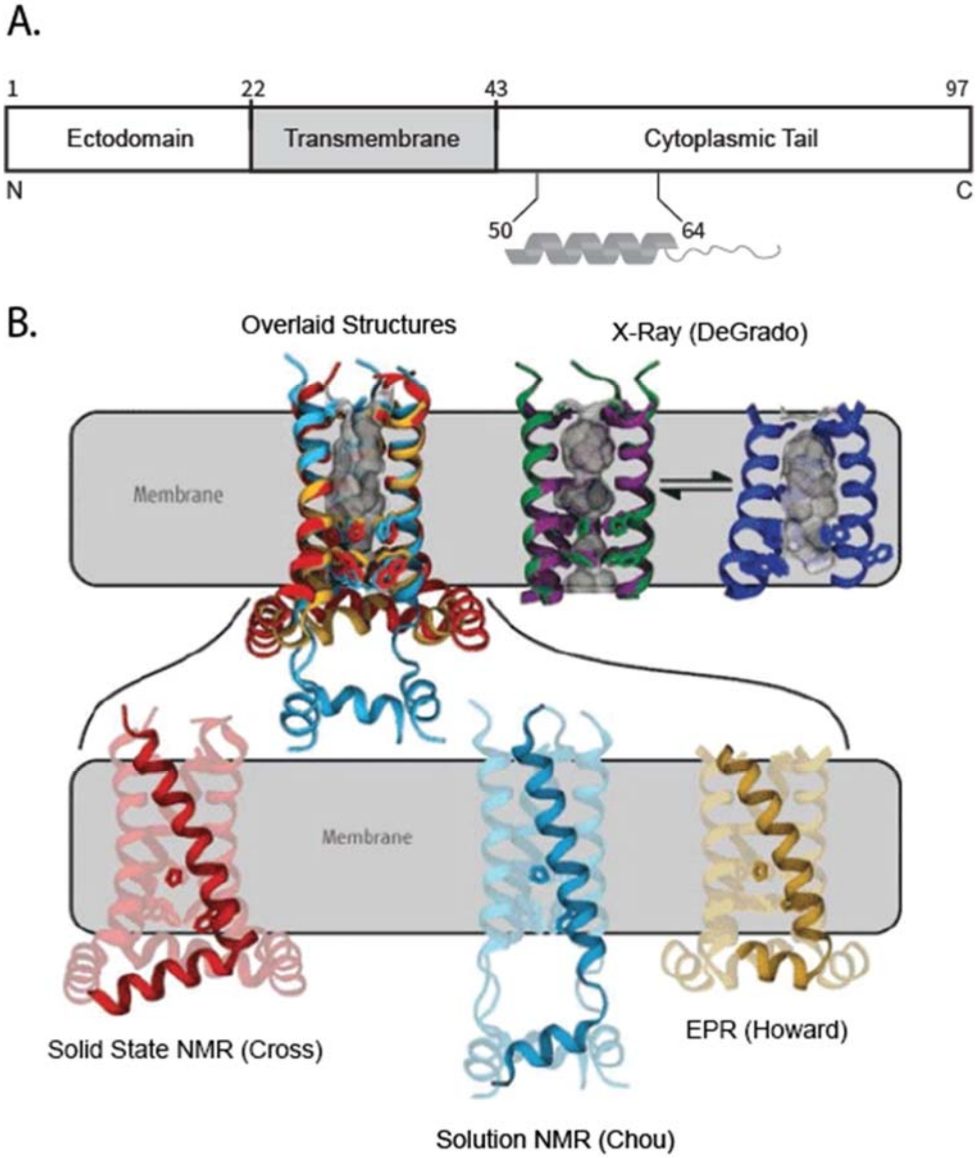

**Figure 1.2. M2 domain map and published structures.** (A) Domain map of the M2 protein showing ectodomain, transmembrane region, and C-terminal domain. Ribbon representation of C-terminal amphipathic helix shown. (B) Previously published structures of M2 solved by different techniques. Structure solved by solid state NMR (red and purple),[12] solution NMR (light blue),[13] X-ray crystallography (green and dark blue)[14-16] and EPR (yellow).[17] Overlay of bottom structures (left) shows differences in cytoplasmic tail structures. From[18]

## *1.4. The Matrix Protein 1*

M1 is a 252 residue protein, which consists of an N-terminal domain (1-165), and a C-terminal domain (166-252) (Fig. 1.3A).[23] In a viral particle, M1 forms a matrix layer associated with the viral envelope that stabilizes NA and HA and aids in maintaining the structural integrity of the virus. The structure of the N-terminal domain of M1 has been determined at both acidic and neutral pH via crystallographic methods, but a full-length crystal structure has not been solved.[23–26] The crystal structure of the M1 N-terminal domain at neutral pH is shown in Figure 1.3B. The highly charged surface of M1 has led to a model of M1 as a 'brick' with an acidic face, a basic face, and a hydrophobic pocket (Fig. 1.3C-D**)**.[23,24,27]

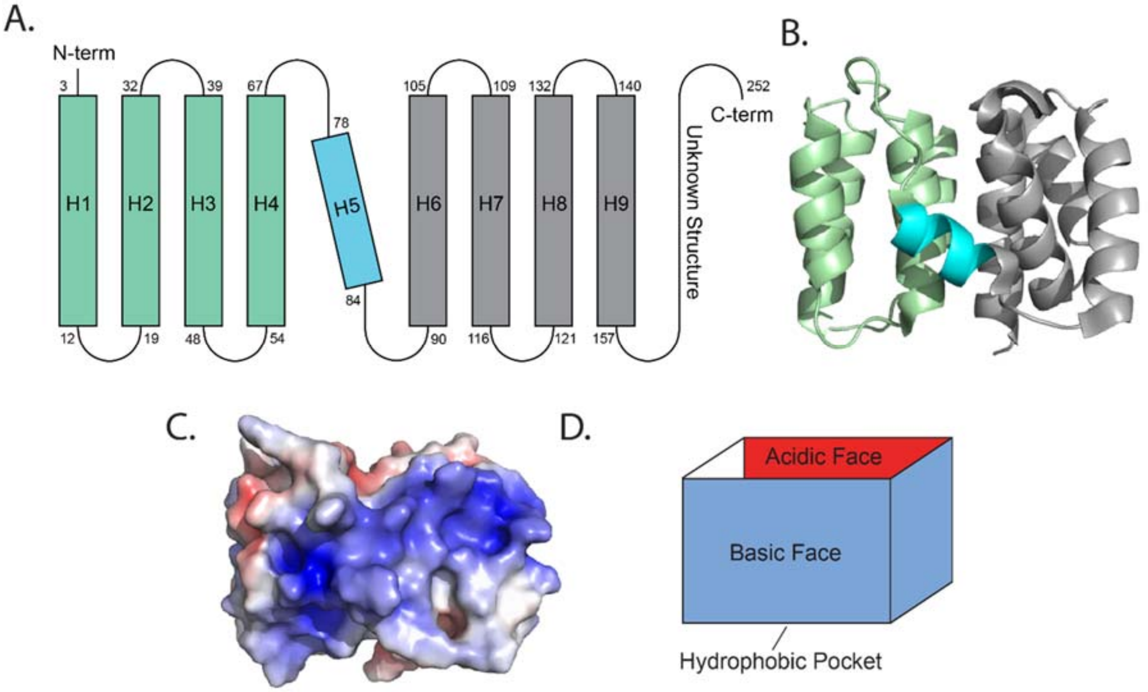

**Figure 1.3. M1 domain map and structure.** (A) Domain map of the M1 protein. (B) Ribbon diagram of M1 N-terminal region structure (PDB: 1EA3). (C) Electrostatic surface of M1 showing basic face (PDB: 1EA3). (D) Cartoon representation of M1 N-terminal domain as a 'brick' with an acidic face, a basic face, and a hydrophobic pocket.

There is small-angle X-ray scattering (SAXS) data and a corresponding model for the full-length protein, which shows a flexible and disordered C-terminal domain and an N-terminal consistent with solved crystal structures.[28] The N-terminal and middle domains consist of two 4 α-helix bundles and a connecting α-helix.[23–26] The failure to successfully crystallize full-length M1 has been attributed to a protease-sensitive loop connecting the middle and C-terminal domains, and intrinsic disorder in the C-terminal region —though circular dichroism has suggested that the C-terminal domain may have α-helical structure.[24]

The M1 protein's N-terminal domain has been suggested to be the primary region involved in interaction between M1 and M2. In their 2018 study, Liu et. al identified mutations in M1 (residues 73, 94, 135, 136, 138, and a double mutant 93/244) that restored virus infectivity in the presence of an M2 mutant (Y76A) that causes greatly reduced virus infectivity, with little effect on viral budding. These M1 mutations were located primarily in the M1 protein's N-terminal domain and could potentially be involved in interaction with the M2 protein.[29] This study of the M2 protein's interaction with M1 utilizes an N-terminal domain construct of the M1 protein (residues 1-165).

### *1.5. Interaction Between Matrix Protein 1 and 2*

Both M1 and M2 have been shown to have roles in the determination of virus morphology and are required for efficient genome packaging.[30–34] Previously, the C-terminal domain of M2 has been shown to have critical roles in both viral budding and the packaging of the viral genome.[19,34,35] An interaction between M1 and M2 has been proposed to facilitate viral assembly.[10]

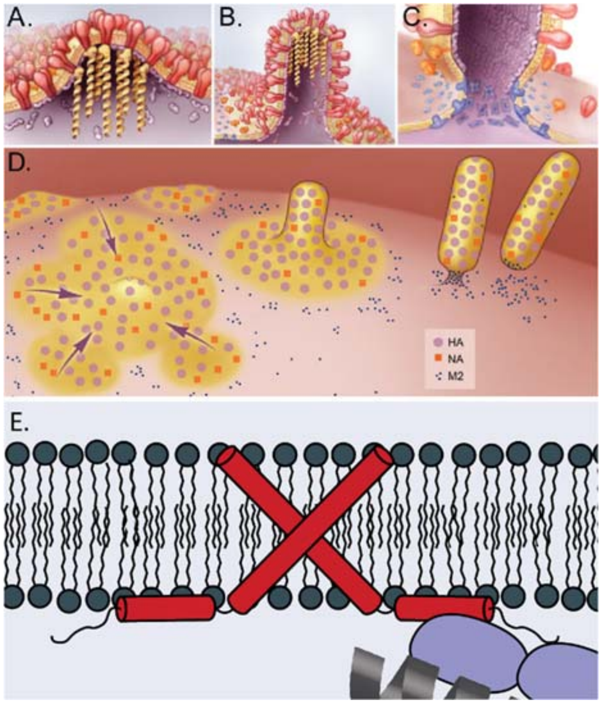

**Figure 1.4. A model for influenza viral assembly and budding.** (A) The viral glycoproteins, HA and NA, cluster at the budozone. M1-vRNP complexes are recruited to the budding site by viral membrane proteins. (B) The new virus is elongated by M1 oligomerization. (C) M2 protein (blue) clusters at the neck of the new virus and create the curvature necessary for scission and virus release. (D) Overview of the viral assembly and budding process. Viral proteins cluster at the budding site, where the new virus elongates outward and is released by membrane scission mediated by the M2 protein. Adapted from[10] (E) Cartoon model of a hypothetical interaction between M1 (purple) and M2 (red) in which M1 is recruited to the budozone.

Genetic evidence supports an interaction between the two proteins. Zebedee and Lamb showed that influenza A viruses with mutations in the M2 cytoplasmic tail and mutations in the M1 protein could escape M2 antibodies, suggesting an interaction between the two proteins.[36] Similarly, Liu et. al investigation of revertant influenza A viruses showed that M1 mutations increased viral budding even without M2, but the extent of infectivity restoration was still dependent on the presence of the M2 protein's cytoplasmic tail (residues 71-97).[29] Liu et. al concluded that their findings support a model in which the identified M1 mutations drive viral budding, with the M2 protein's C-terminal domain playing an important part in genome packing. Essentially, a virus assembly in which budding and genome packaging are separate stages, with budding able to occur without packaging.[29] These findings suggest that M1-M2 binding pulls M1-vRNP complexes to the budozone where both M1 and M2 play a part in the budding process (Fig. 1.4).[10]

Truncations of the M2 protein have been shown to lead to decreased viral infectivity.[19,34,35] Deletion of the last 28 residues from the M2 protein's C-terminus causes a fourfold decrease in particle formation and a 1,000-fold decrease in infectivity.[34] M2 truncations show a decrease in the incorporation of vRNP into newly formed viruses.[19,34] This reduced incorporation has been posited to be due to reduced M1-M2 interaction. The M2 protein has been utilized to target M1 to the plasma membrane. Wang et. al reported that M1 lacked an inherent membrane-targeting signal, and alone was not sufficient to form virus-like particles (VLPs). But when M1 was coexpressed with wild-type M2, it was targeted to the membrane and produced VLPs with M1 incorporated. When coexpressed with an M2 mutant with no cytoplasmic tail, M1 failed to shift to the membrane and produce VLPs.[37]

To narrow the potential candidate regions on M2 that engage in M1 binding, scanning alanine mutagenesis has been utilized. In a VLP system, Chen et. al reported that tri-alanine mutants (residues 71-73 or residues 74-76) of M2 showed reduced infectivity and reduced M1 incorporation into VLPs. However, truncated M2 (residues 1-71) did not affect M1 incorporation and genome incorporation. Chen et. al hypothesized that overlapping mechanisms may be responsible for this trend.[38]

Direct physical interaction between the M1 and M2 proteins has been reported. The M1 protein can be pulled down by the full-length M2 protein, but not truncations or an M2 construct with only residues 70-97.[35,38] This failure of M2 residues 70-97 to pull down M1 could be attributed to an M1 binding site between residues 45-69 or due to the conformation of residues 70-97 without the remainder of the protein.[35] Wild-type M1 and M2 have been shown to coimmunoprecipitate, with coimmunoprecipitation reduced between wild-type

M1 and tri-alanine mutant M2.[38] These findings suggest that M1 and M2 may undergo binding through multiple sites on the M2 cytoplasmic tail with a specific binding site including the conserved M2 residues 71-77. Redundancies in the mechanism for M1 recruitment to the membrane are potentially responsible for the preservation of an essential interaction between M1 and M2, an interaction which is posited to facilitate the delivery of the viral genome to the viral budding site.[10,35,38]

Though evidence supporting a direct interaction between M1 and M2 exists, there is currently no atomic level detail clarifying their interaction and no proposed model for the structure of that interaction. In the current study, we employ the use of site-directed spin label electron paramagnetic resonance (SDSL-EPR) spectroscopy to gain atomic level insight into the interaction between the M1 and M2 proteins by analyzing change in the M2 protein's cytoplasmic tail dynamics and structure upon binding the M1 protein.

### *1.6. Methods for Studying the Structure and Dynamics of Membrane Proteins*

The use of SDSL-EPR to study membrane proteins addresses some of the drawbacks to techniques used more frequently. NMR spectroscopy and X-ray crystallography are the two most commonly used techniques for investigating the structure of proteins. Both methods can produce highly detailed three-dimensional structures, and while X-ray crystallography can produce only static structures, NMR can produce dynamic information as well. Membrane proteins, however, can pose a challenge for both. Crystallizing membrane proteins is problematic, due to their hydrophobicity and flexibility.[39] NMR can be limited by size, as the spectra of protein-lipid ensembles can be difficult to deconvolute.[40] SDSL-EPR can be used to analyze membrane protein structure in more physiologically relevant lipid bilayer systems and provide dynamic information about the system. EPR spectroscopy is also highly sensitive. It requires low quantities of sample (compared to X-ray crystallography) and is about 1,000 times more sensitive than NMR spectroscopy, due to the energy frequencies involved.[40–42] EPR spectroscopy can also provide multiple types of information including distances between paramagnetic moieties, mobility, and accessibility to paramagnetic relaxation agents.

# Chapter 2 : Electron Paramagnetic Resonance Spectroscopy of Membrane Proteins

Electron paramagnetic resonance (EPR) spectroscopy is a powerful method for studying the structure and dynamics of membrane proteins. This chapter will briefly outline the basics of EPR, the use of EPR in site-directed spin labeling (SDSL), and some of the information that can be obtained using SDSL-EPR. For further applications of EPR in biochemical contexts and in the study of proteins using SDSL-EPR, the reader is referred to a number of recent reviews.[40,43–45]

## *2.1. Electron Paramagnetic Resonance Spectroscopy*

EPR spectroscopy relies on the intrinsic magnetic moment, $s$, and the spin quantum number of a single electron, denoted as $m_s$. Paired electrons have a net moment of zero, while an unpaired electron occupies one of two spin states: $m_s = +\frac{1}{2}$ or $m_s = -\frac{1}{2}$. These two spin states are degenerate in the absence of an external magnetic field. In the presence of an external magnetic field, the states are split into higher and lower energy levels. This is known as Zeeman splitting (Fig. 2.1). The energy difference between the two spin states is proportional to the magnitude of the applied external magnetic field and is described by Equation 1:

$$\Delta E = h\nu = g_e \mu_B B_0 \qquad (1)$$

where $g_e$ is the g-factor for the electron, $\mu_B$ is the Bohr magnetron, and $B_0$ is the strength of the magnetic field.[41,46] Transitions between energy states are typically detected by sweeping over the frequency of electromagnetic radiation until the energy difference is matched and an absorbance peak is registered. However, EPR spectra are typically generated by holding frequency constant and sweeping the magnetic field until the energy gap between spin states matches the frequency. Additionally, EPR spectra are generally recorded as the first derivative of the absorbance spectra as it provides greater sensitivity and a better signal to noise ratio.[41,42,47]

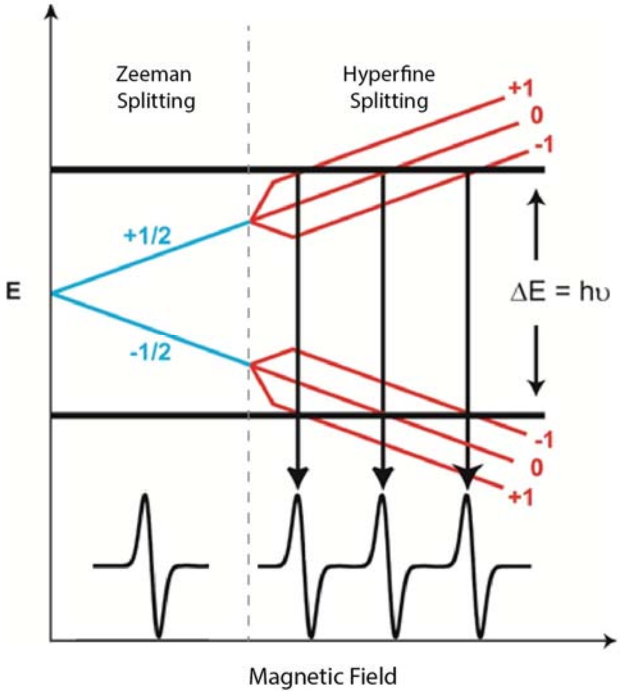

**Figure 2.1. Nondegeneracy of electron spin states produces EPR signal.** In the presence of an external magnetic field, a radical's spin states are not degenerate, producing Zeeman splitting. The signal can be further split by neighboring nuclei, producing a hyperfine splitting pattern. Varying the strength of the magnetic field until the energy difference of a chosen power is matched produces transitions between spin states. Energy transitions can be detected and are typically displayed as the first derivative of the absorbance spectrum.

If the nuclei surrounding the unpaired electron have non-zero nuclear spin, the electron's spin states can be split again by neighboring nuclei in what is known as hyperfine splitting. This splitting produces additional energy states and thus additional peaks in the EPR spectrum. The number of additional energy states correspond to the magnetic moment, *S*, of the splitting nuclei in the relationship $2S+1$. For example, the splitting pattern of a nitroxide radical, in which the radical is centered on a single nitrogen atom, can be seen in Figure 2.1, where the $^{14}$N nucleus with $S = 1$ splits the electron spin states into three sub-states, $m_I = -1, 0, 1$. According to the quantum mechanical selection rules, only transitions between energy levels with $\Delta m_s = \pm 1$ and $\Delta m_l = 0$ are allowed, so three peaks are observed in the line shape of a nitroxide radical (Fig. 2.1).

### *2.2. Site-Directed Spin Label EPR Spectroscopy*

The nitroxide radical often provides the basis for site-directed spin labeling EPR spectroscopy.[43,44] The commonly used nitroxide radical spin label (1-oxyl-2,2,5,5-tetramethyl-Δ3-pyrroline-3-methyl)-methanethiosulfonate (MTSL) is employed in this study. In SDSL-EPR, a spin label is installed on a specific protein residue. For the installation of MTSL, a single cysteine mutation is introduced at the residue of interest in an otherwise cysteine-less protein. The cysteine sulfhydryl forms a disulfide linkage to MTSL, creating what is known as the R1 side chain (Fig. 2.2). This side chain is sensitive to the local environment, providing residue-specific information.[48] This information includes side chain mobility and accessibility to paramagnetic relaxation agents.

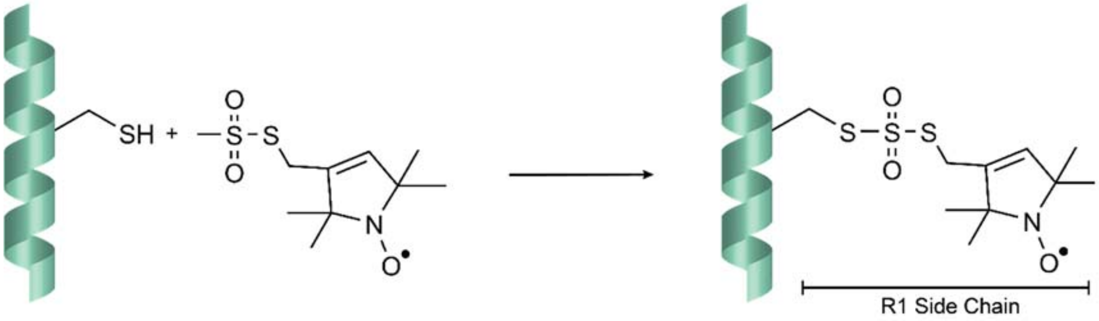

**Figure 2.2. Site-directed spin labeling reaction**. A single cysteine mutation is introduced at the site of interest in an otherwise cysteine-less background and a nitroxide spin label (MTSL) is attached via a disulfide bond. This reaction produces the R1 side chain.

### *2.3. Site Mobility from EPR Line Shape*

The EPR line shape produced by a nitroxide radical spin label can provide information on the mobility of the R1 side chain. The hyperfine splitting of the nitroxide is orientation dependent and the observed spectrum is made up of the spectra of the different orientations. The motion of the overall protein determines the way the line shape is assembled from individual orientation spectra. The overall protein motion can fall into a motional model that ranges from the rigid limit (immobile), to the isotropic limit (extremely fast tumbling). Under an isotropic model, the orientation spectra can be averaged to create the observed line shape, while under the other models the observed line shape is a superposition of the orientation spectra. The greater contribution of the slower orientation spectrum causes observed line shape breadth. Figure 2.3A shows the line shapes of a nitroxide radical spin label in solution (top), affixed to a protein (middle), and frozen (bottom). The three peak line shape broadens as the mobility of the spin label decreases.

The breadth of the line shape can be quantified using the semi-empirical parameter $\Delta H^{-1}$, the inverse of the central peak width (Fig. 2.3B**)**.[43,49] However, further quantitative information about nitroxide radical dynamics can be provided by spectral simulation. The EPR line shape can be fit using software like EasySpin from which spectral parameters can be extrapolated, including correlation time.[50] Correlation time, the time that it takes for the molecule to rotate one radian, measures molecular tumbling and can function as a measure of mobility. A motional model must be chosen to extract the correlation time and EasySpin offers different functions for different motional models. Figure 2.3C shows simulated EPR line shapes for a nitroxide spin label with different correlation times: 0.1 ns for the more narrow spectrum (left) and 3.0 ns for the broader spectrum (right). [51,52]

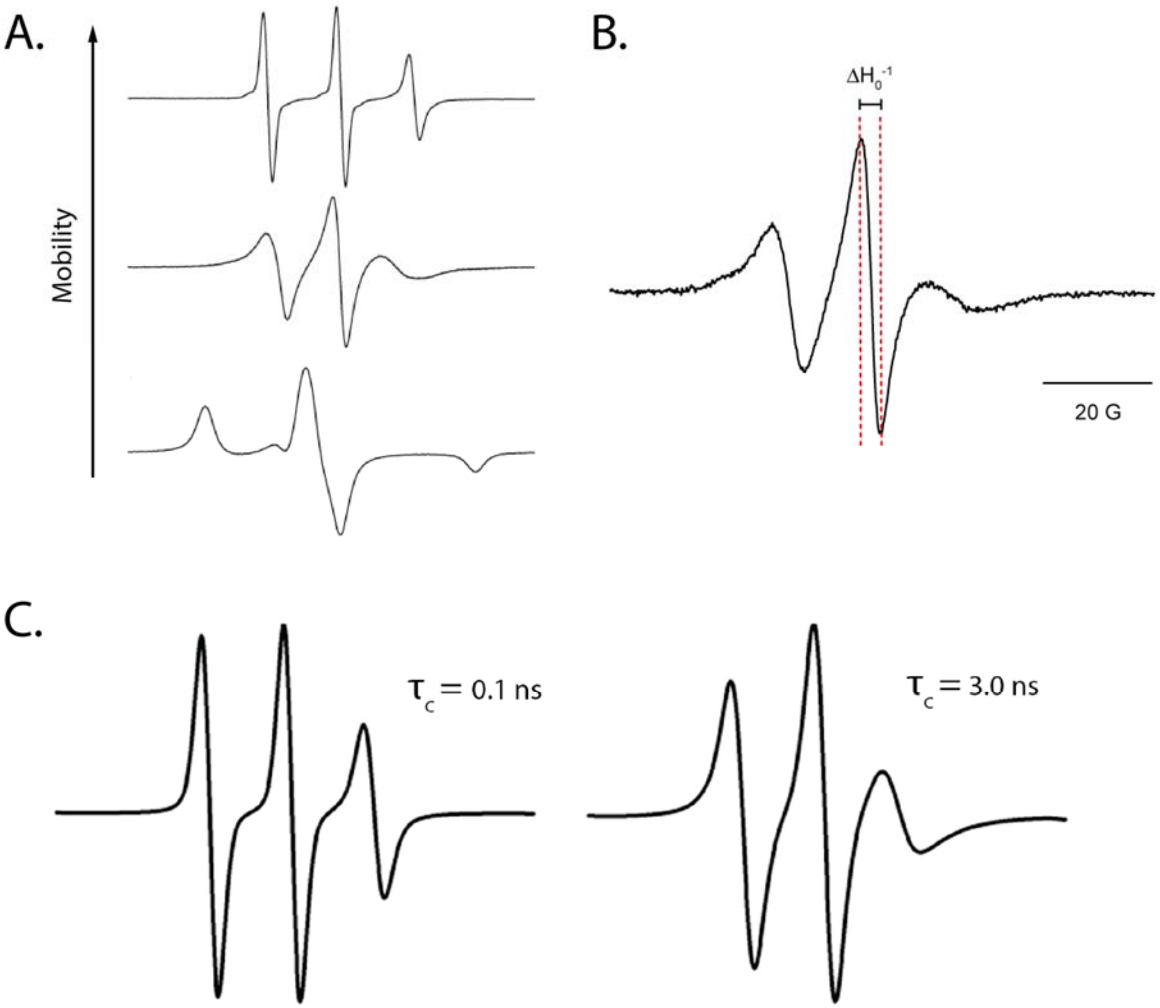

**Figure 2.3. Residue-specific mobility information from the EPR line shape.** The breadth of the EPR line shape gives information about the mobility of the R1 side chain. (A) Narrow line shapes are more mobile. From top to bottom: nitroxide spin label in solution, affixed to a protein, and frozen. (B) Spectral breadth can be quantified using the semi-empirical parameter $\Delta H^{-1}$, the inverse of the central line width. (C) Physical parameters can be extracted using simulated spectra. The correlation time, $\tau_c$, can function as a measure of relative mobility, with higher correlation times corresponding to slower motion. Right spectrum shows higher correlation time and broader line shape compared to left. Adapted from[52]

### *2.4. Oxygen Accessibility from EPR Power Saturation Studies*

In addition to site-specific information about mobility, SDSL-EPR can provide information about a site's accessibility to a paramagnetic relaxation agent through power saturation experiments. These experiments make use of the linear relationship between the amplitude of the EPR signal and the square root of the incident microwave power. As power increases, the intensity of the signal also increases until the rate at which the radicals are excited is equal to the rate at which the radicals relax back down. At that point there is no increase in signal amplitude with microwave power—the signal is saturated.[53] The linear hypothetical unsaturated intensity (black line) is depicted in Figure 2.4A, along with actual saturated intensity without a relaxation agent (black line with black circles). The actual relationship between the square root of microwave power and intensity becomes less linear at increasing powers and eventually intensity plateaus.

In the presence of a paramagnetic relaxation agent, the relaxation rate is increased, as the spin label engages in Heisenberg exchange with the relaxation agent.[54] This increased relaxation rate increases the power at which the EPR signal is saturated. The central line amplitude of the EPR signal can be plotted against the square root of microwave power and fit according to Equation 2:

$$A = I \cdot P^{\frac{1}{2}} \left[ \frac{1+\left(2^{\frac{1}{\varepsilon}}-1\right)P}{P_{1/2}} \right]^{-\varepsilon} \tag{2}$$

where $A$ is the amplitude of the central line, $I$ is a scaling factor, $P$ is the incident power, ε is a factor measuring line homogeneity, and $P_{1/2}$ is the power at which line amplitude is half that of the theoretical unsaturated amplitude (Fig. 2.4A).[53] The $P_{1/2}$ power saturation parameter can be found for the sample with no paramagnetic relaxation agent and compared to that of the sample in the presence of a paramagnetic relaxation agent. The produced difference is the $\Delta P_{1/2}$ value, which quantifies the spin label's accessibility to a paramagnetic relaxation agent.[53]

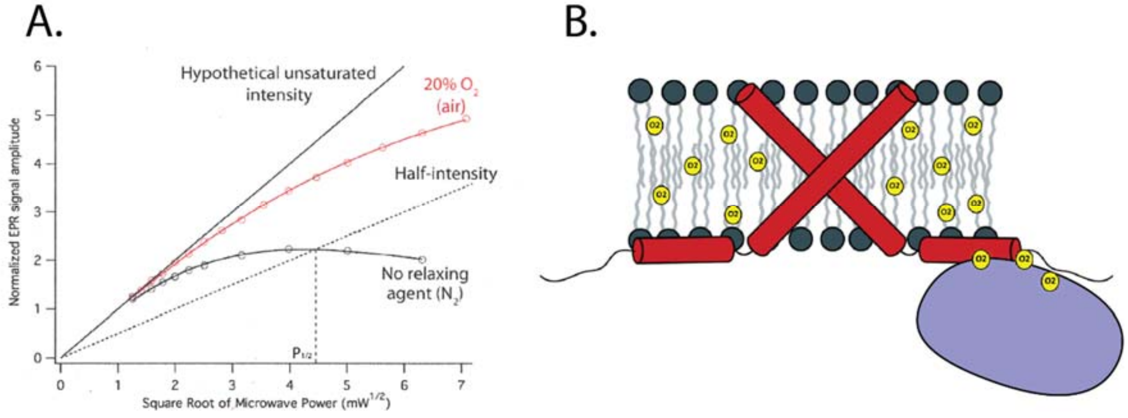

**Figure 2.4. Residue-specific oxygen accessibility from power saturation experiments. (**A) The EPR signal intensity has a positive linear relationship with the square root of microwave power. At sufficiently high power, the signal becomes saturated as the number of net spin state transitions become zero. Black line shows the hypothetical unsaturated intensity as a function of the square root of microwave power. Black line with circles shows actual intensity that becomes saturated at high power. In the presence of paramagnetic oxygen, EPR signal takes higher powers to saturate (shown in red). The $P_{1/2}$ value can be used as a quantitative measure of saturation. (B) Cartoon of hypothetical M1 (purple) and M2 (red) binding and the partitioning patterns of oxygen. An increase in an M2 residue's oxygen accessibility could be ascribed to increased membrane depth or the formation of a hydrophobic interface near that residue.

Oxygen is one of the most commonly used paramagnetic relaxation agents.[40,53] Small and hydrophobic, oxygen segregates away from the aqueous phase. Oxygen accessibility can correspond to membrane depth, as it partitions into the bilayer. Oxygen can also sequester itself into hydrophobic interfaces within or between proteins. Figure 2.4B shows a cartoon of the M1-M2 system in which oxygen accessibility could be reflective of a residue's increased membrane depth or the creation of a hydrophobic pocket at a hypothetical M1-M2 interface caused by M1-M2 binding.

# Chapter 3 : Preparation of Reconstituted M2 Protein Constructs

## *3.1. Mutagenesis and Expression of M2 Protein Constructs*

Existing Howard lab M2 protein constructs with single cysteine mutants were utilized. Constructs consisted of A/Udorn/M2 with a C-terminal $His_6$ tag, the mutations W15F, C17S, C19S, and C50S, and single cysteine substitutions at sites of interest. All single cysteine mutations were introduced via the QuikChange Lightning Site-Directed Mutagenesis Kit according to manufacturer's protocol (Agilent Technologies). Plasmid sequences were verified using Sanger sequencing (Genewiz Inc.). Plasmids were then transformed into Overexpress$^{TM}$ C43 (DE3) Competent cells (Lucigen) for protein expression, according to manufacturer's protocol.

For each M2 construct, a starter culture of 5 mL of Luria broth (LB) solution with 100 µg/mL ampicillin was inoculated with transformed *E. coli* from glycerol cell stocks and shaken overnight at 180 rpm in 37°C. After incubation, the 5 mL starter culture was diluted with 1 L of LB broth solution with 100 µg/mL ampicillin. Growth of *E. coli* was accomplished at 180 rpm in 37°C and monitored by the liquid culture's optical density at 600 nm ($OD_{600}$). At an $OD_{600}$ of approximately 0.7-1.2, overexpression of recombinant M2 was induced by 1 mM isopropyl β-D-1-thiogalactopyranoside (IPTG). Overexpression was allowed to proceed for an additional two hours, then $OD_{600}$ was monitored to observe slowed growth. Once $OD_{600}$ was observed to increase less than 0.1 in 30 minutes, cells were harvested by centrifugation at 4000 rpm at 4°C for 30 minutes. The supernatant was discarded, and the cell pellet was resuspended in 50 mL LB broth solution followed by transfer to four 50 mL Falcon tubes. The resuspended cell pellet was again pelleted at

4000 rpm at 4°C for 30 minutes and the supernatant was again discarded. Pelleted cells were stored at -80°C for later lysis and M2 purification.

### *3.2. M2 Purification and Spin-labeling*

For each M2 protein construct, a cell pellet from ¼ L of growth was incubated on ice with 9.5 mL M2 Lysis buffer (50 mM Tris pH 8.0, 30 mM octyl β-D-glucopyranoside (OG), 150 mM NaCl, 0.2 mg/mL DNase, 0.25 mg/mL lysozyme, and 50 mM AEBSF) for 20 minutes. After incubation, the cell pellet was resuspended by vortexing until homogeneous. To lyse cells, the resuspended cell pellet was then sonicated on ice at 20% amplitude, for 20 minutes in a 1 sec on / 1 sec off cycle. The lysate was then immediately centrifuged at 16,000 rpm for 30 minutes at 4°C to separate cellular debris. The post-lysis pellet was discarded, while post-lysis supernatant was prepared for nickel affinity chromatography by the addition of 7 mM β-mercaptoethanol (BME) and 20 mM imidazole. The supplemented post-lysis supernatant was then nutated with 0.5 mL HisPur$^{TM}$ Ni-NTA resin (ThermoScientific) for 30 minutes at room temperature. The column was washed with 10 column volumes each of M2 Wash I (50 mM Tris pH 8, 150 mM NaCl, 30 mM OG, 20% v/v glycerol), M2 Wash II (50 mM Tris pH 8, 30 mM OG, 20% v/v glycerol), and M2 Wash III (50 mM Tris pH 8, 30 mM OG, 20% v/v glycerol, 20 mM imidazole). To spin-label the protein, 1.8 mM MTSL (10-fold molar excess) in 2 column volumes M2 Wash III was applied to the column and spin-labeling reaction was allowed to proceed for 24-48 hours.

After spin-labeling, the column was washed with 10 column volumes of M2 Wash II and protein was eluted off the column with M2 Elution Buffer (50 mM Tris pH 8, 30 mM OG, 300 mM imidazole, 20% v/v glycerol). The eluted protein was buffer-swapped into M2 Desalting Buffer (50 mM Tris pH 8, 30 mM OG) via PD-10 Desalting Column (GE Healthcare Life Sciences).

The EPR spectrum of pooled post-PD-10 M2 protein was acquired to verify signal and check for free excess spin-label. If the spectrum of the pooled post-PD-10 protein showed evidence of free spin, a second run through the PD-10 was performed. The purity of pooled post-PD-10 protein was verified via sodium dodecyl sulfate–polyacrylamide gel electrophoresis (SDS-PAGE) (Fig. 3.1). The M2 protein appears as a monomer band (15 kDa) with a less intense dimer band (25 kDa) on an SDS-PAGE gel.

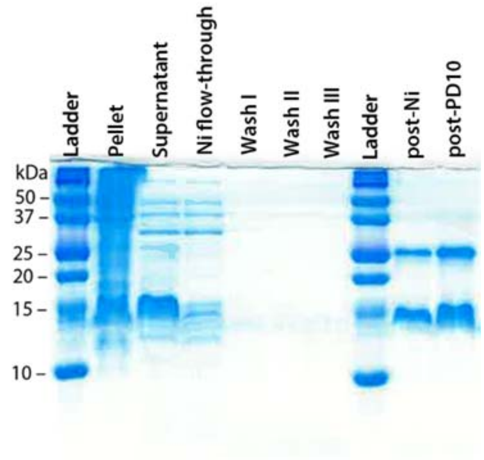

**Figure 3.1. Representative gel for M2 purification.** SDS-PAGE tracks M2 throughout successful purification of M2 V68C mutant. Monomeric M2 appears as a band at approximately 15 kDa and dimeric M2 appears as a band at approximately 25 kDa.

*3.3. Reconstitution of M2 Protein Constructs into Proteoliposomes*

Purified M2 protein was reconstituted into 4:1 1-palmitoyl-2-oleoyl-sn-glycero-3-phosphocholine:1-palmitoyl-2-oleoyl-sn-glycero-3-[phosphor-rac-(1glycerol)] (POPC:POPG) bilayers at a 1:500 protein:lipid ratio. Lipid films were solubilized in Extruder Buffer (50 mM Tris pH 8, 100 mM KCl, 1 mM ethylenediamine-*N,N,N’,N’*-tetraacetic acid (EDTA)) and extruded 15 times through a 20 μm filter using an Avanti Mini-Extruder to homogenize the vesicle sizes. OG detergent was added to a concentration of 30 mM and the lipid-detergent solution was equilibrated for 30 minutes. Purified M2 protein was added to a 1:500 protein lipid ratio and additional Extruder Buffer was added to dilute OG concentration to 15 mM, below the critical micelle concentration. Six additions of 50 µL of a degassed slurry of hydrophobic polystyrene beads (BioBeads SM-2, Bio-Rad) in Extruder Buffer were made over at least 90 minutes to facilitate the removal of detergent. BioBeads were removed and proteoliposomes were pelleted at 90,000 rpm for 1 hour at 4°C in the TLA-100 rotor of an Optima-MAX-TL ultracentrifuge (Beckman-Coulter). To concentrate the proteoliposomes, all pellets were combined and resuspended in approximately 200 µL of supernatant. The concentrated proteoliposome solution was re-pelleted under the same centrifugation settings and stored separately as pellet and supernatant at 4°C.

## Chapter 4 : Optimization of M1 Expression and Purification

### *4.1. Plasmid for Matrix Protein 1*

A plasmid consisting of the N-terminal domain of M1 (residues 1-165) with an N-terminal His$_6$ tag subcloned into a pET30b vector (Novagen) was obtained from the Xie group at the United States Food and Drug Adminstration.[23] Plasmid was amplified in XL Gold Ultracompetent cells (Agilent Technologies), purified via QIAprep Spin Miniprep kit according the manufacturer's protocol (Qiagen) and transformed into cells for protein expression, as described in Chapter 3.

### *4.2. Initial Attempt to Express Soluble M1 Protein*

Expression of the M1 construct was initially attempted at 30°C in *E. coli* induced with 0.5 mM IPTG. Expression conditions were drawn from the Xie group.[23] M1 protein was successfully expressed, as seen in Figure 4.1**,** where the addition of an 18 kDa band matching the molecular weight of M1 can be seen from pre- to post-induction.

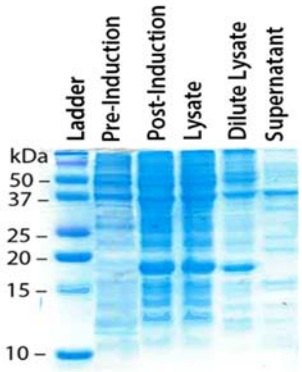

**Figure 4.1. SDS-PAGE analysis of initial M1 protein lysis attempt.** M1 construct appears as a band of approximately 18 kDa. Pre- and post-induction samples show the successful overexpression of M1. Post-lysis supernatant sample shows no M1 protein band which is indicative of M1 partitioning into post-lysis pellet. No soluble M1 protein was produced in this lysis attempt.

Lysis was attempted via sonication using established protocols for lysis of cells containing the M2 protein. Lysate was spun down to remove cellular debris. SDS-PAGE showed a band matching the molecular weight of the M1 protein construct in the lysate and the post-lysis pellet, but not the post-lysis supernatant (Fig. 4.1**)**. This distribution of protein was potentially indicative of M1 protein aggregation into inclusion bodies (Fig. 4.1). As a viral capsid protein, M1 presents a likely candidate for aggregation and has been previously observed to form inclusion bodies.[55]

### *4.3. Inclusion Bodies*

Inclusion bodies are protein aggregates. In recombinant protein overexpression, these aggregates consist primarily of the overexpressed protein. Inclusion bodies are often observed for viral capsid proteins, and proteins expressed at high temperatures, high inducer concentrations, and under strong promoter systems. Expressed protein partially folds or misfolds, forming stable aggregates within the cell. There are numerous reported methods to obtain soluble protein when inclusion bodies form.[56–59]

Growth and induction can be optimized to yield soluble protein with or without inclusion bodies. Inducer concentration and temperature are lowered to slow protein expression. Even with the formation of inclusion bodies, there may be sufficient soluble protein.

If growth cannot easily be optimized, inclusion bodies can be extracted, and protein can be solubilized. The first step to purify protein from inclusion bodies is lysis and centrifugation. The supernatant can be discarded, and the pellet will be disrupted and washed multiple times with detergent to remove lipid and membrane proteins. A final wash in DI water or buffer serves to rinse and remove excess detergent.

Then the washed inclusion bodies are solubilized. There are several techniques to extract protein from inclusion bodies which generally involve the addition of some sort of agent to solubilize the protein. These can be non-denaturing, mild, or denaturing solubilization agents. Some non-denaturing agents include sarcosyl, DMSO, and n-propanol. Mild solubilization conditions include high pH, higher concentrations of n-propanol, and low concentrations of urea. Protein can also be completely denatured using high concentrations of guanidine hydrochloride or urea.[57,60–62]

Once the protein is completely solubilized, cellular debris is pelleted out and the supernatant is often filtered to remove any unpelleted cell wall debris. The protein must then be isolated and refolded, in the case of mild solubilization or denaturing solubilization agents.

Refolding requires the removal of the denaturant and is often accomplished via dialysis or serial dilution. Refolding can also be done on a column. Protocols for protein refolding on nickel affinity columns have been reported, in which bound $His_6$-proteins are washed with detergent and rinsed with cyclodextrin to remove excess detergent.[63,64] On-column protein refolding has also been reported using decreasing denaturant concentration washes.[59,65]

### *4.4. Further Attempts to Express Soluble M1 Protein*

To avoid optimizing extensive inclusion body purification protocols, growth temperature and inducer concentration were varied to produce soluble M1 protein. Expression was attempted at 37°C, 30°C, and 18°C, with inducer concentrations of either 1 mM, 0.5 mM, or 0.4 mM. However, none of the conditions tested produced soluble M1 under the sonication lysis protocol.

An inclusion body protocol was designed for the M1 protein drawing from several published methods.[59,60,62,66] The procedure is outlined in Figure 4.2**.** The most commonly used solubilization method was utilized: high concentrations of guanidine hydrochloride.

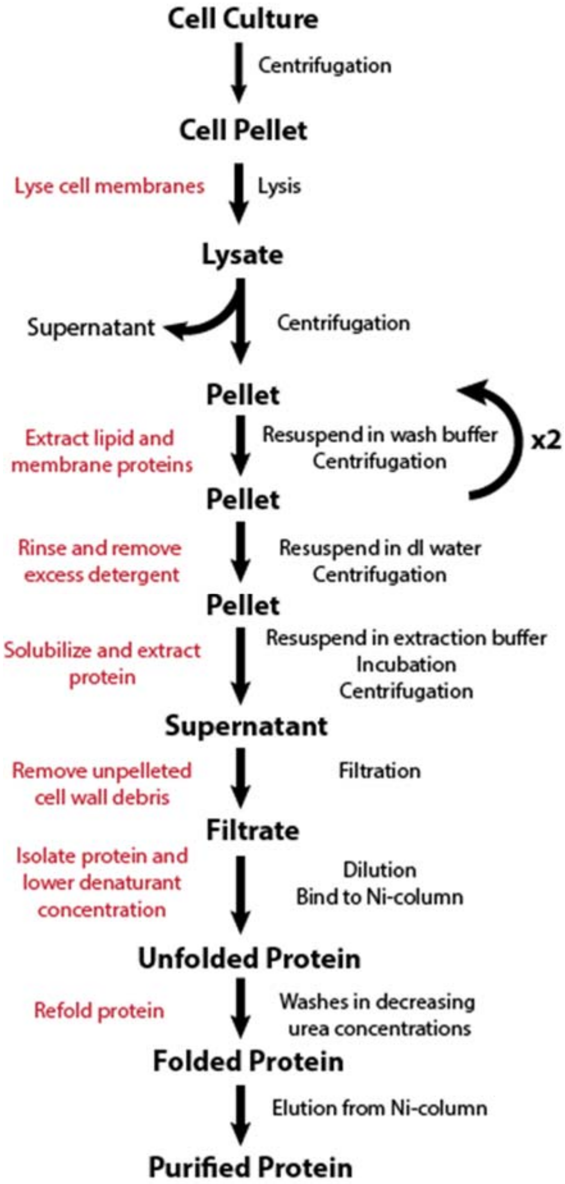

**Figure 4.2. Outline of protein extraction from inclusion bodies**. Inclusion bodies are stable aggregates of expressed proteins. Protein extraction consists of isolating inclusion bodies, solubilizing and denaturing protein, and protein refolding.

After lysis by sonication and centrifugation, the resulting pellet was washed in detergent and de-ionized water. Inclusion bodies were then dissolved in 6 M GuHCl, spun down, and filtered to remove any unpelleted large cellular debris. The solution was then diluted to 4 M GuHCl and applied to 0.5 mL nickel affinity HisPur$^{TM}$ Ni-NTA resin (ThermoScientific). The column was then washed with decreasing concentrations of urea and eluted with an acidic elution buffer (55 mM $KH_2PO_4/K_2HPO_4/H_3PO_4$ pH 4.0, 0.2 M NaCl, 300 mM imidazole).

However, only a small amount of protein was recovered. This low yield led to the pursuit of alternate inclusion body purification protocols. An existing protocol to purify N-terminal or full-length M1 from inclusion bodies was followed and protein was successfully purified, but still in low yields considering the time requirements of the protocol.[55]

## *4.5. Assessment of Cell Lysis*

Amidst these purification attempts, the SDS-PAGE results proved somewhat concerning. The post-lysis supernatant sample seemed 'emptier' than the comparable sample for M2 purification (not shown). Additionally, a band for M1 appeared in the inclusion body washes (not shown). These observations pointed to an incomplete lysis, which prevented the release of protein from within the cells. An experiment was designed to test whether addition of detergent or a different disruption method would completely lyse the cells (Fig. 4.3). Existing cell pellets grown at 18°C and with 0.4 mM IPTG were utilized. Lysis via sonication with detergent yielded no M1. However, lysis via cell disruptor without detergent yielded M1 in both the post-lysis supernatant and the post-lysis pellet. This supernatant was purified via nickel affinity chromatography, yielding about 0.3 mg for 1/8 of a liter. Subsequently, a 'bulk' purification method was pursued.

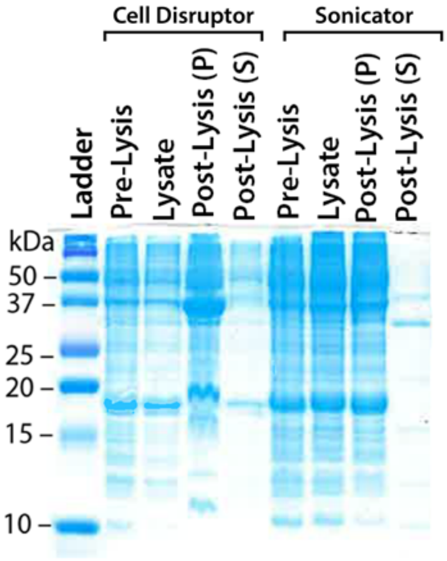

**Figure 4.3. Lysis test for production of soluble M1 protein.** M1 construct appears as a band of approximately 18 kDa. Pre-lysis resuspended pellet and lysate show band for M1 protein. Lysis via cell disruptor produced M1 in the post-lysis supernatant (S) and pellet (P). Lysis via sonication produced M1 only in post-lysis pellet (P), but not soluble M1 in post-lysis supernatant (S). Sonication failed to completely lyse cells.

## *4.6. Expression and Lysis of M1 Protein*

Overexpression for M1 was accomplished at a low temperature over three days. A starter culture of 5 mL of LB broth solution with 50 μg/mL kanamycin was inoculated with transformed *E. coli* from glycerol cell stocks and shaken overnight at 180 rpm in 37°C. After incubation, the 5 mL starter culture was diluted with 1 L of LB broth solution supplemented with 50 µg/mL kanamycin. Growth of *E. coli* was accomplished at 180 rpm in 37°C and monitored by the liquid culture's $OD_{600}$. At an $OD_{600}$ of approximately 0.5, *E. coli* cultures for M1 overexpression were transferred to a shaker at 180 rpm in 18°C. At an $OD_{600}$ of approximately 0.7-1.2, overexpression of recombinant M1 was induced by 0.4 mM IPTG. Overexpression of M1 was allowed to proceed overnight. Cells were harvested in half liter pellets the next morning.

A cell disruptor was utilized to lyse *E. coli* and obtain M1 in the post-lysis supernatant. Additionally, a more intense chemical lysis step was incorporated from a previous protocol for M1 purification.[55] After resuspending the frozen pelleted cells in M1 Lysis Buffer (55 mM $KH_2PO_4/K_2HPO_4/H_3PO_4$ pH 7.5, 0.2 M NaCl), lysozyme was added to a final concentration of 0.3 mg/mL, DNase I to 0.016 mg/mL, and AEBSF to 100 µM. The suspension was nutated for one hour at 4°C, lysed via cell disruptor, and purified via nickel affinity chromatography and size exchange chromatography.

### *4.7. Optimization of M1 Purification*

Purification via nickel affinity chromatography led to partially successful isolation of the M1 protein. For purification, lysate supernatant was first supplemented with 20 mM imidazole and 7 mM BME and then applied to 0.5 mL HisPur$^{TM}$ Ni-NTA resin (ThermoScientific). The binding of the protein to the column was facilitated by nutation for one hour at 4°C. The column was washed with 10 column volumes of M1 Wash I (55 mM $KH_2PO_4/K_2HPO_4/H_3PO_4$ pH 7.5, 0.2 M NaCl, 20% v/v glycerol) and M1 Wash II (55 mM $KH_2PO_4/K_2HPO_4/H_3PO_4$ pH 7.5, 0.2 M NaCl, 20 mM imidazole). Protein was eluted from the column in 0.5 mL fractions with buffer (55 mM $KH_2PO_4/K_2HPO_4/H_3PO_4$ pH 4.0, 0.2 M NaCl, 300 mM imidazole). Analysis of nickel affinity chromatography via SDS-PAGE showed high molecular weight bands in the first six fractions along with the majority of the M1 protein (Fig. 4.4A).

To optimize nickel column purification, an imidazole gradient was utilized. Successive elutions at 50 mM, 150 mM, 200 mM, and 300 mM imidazole separated the high molecular weight impurities from the majority of the M1 protein (Fig. 4.4B). Initial elutions with impurities contained only a small amount of M1 protein. Small 50 µL aliquots were removed from each fraction for analysis of protein concentration and fraction purity. All fractions were flash-frozen and stored at -80°C. Before experimentation, fractions verified to contain no impurities by SDS-PAGE were further purified by size exchange chromatography on a Superdex 75 Increase 10/300 GL column (GE Healthcare Life Sciences).

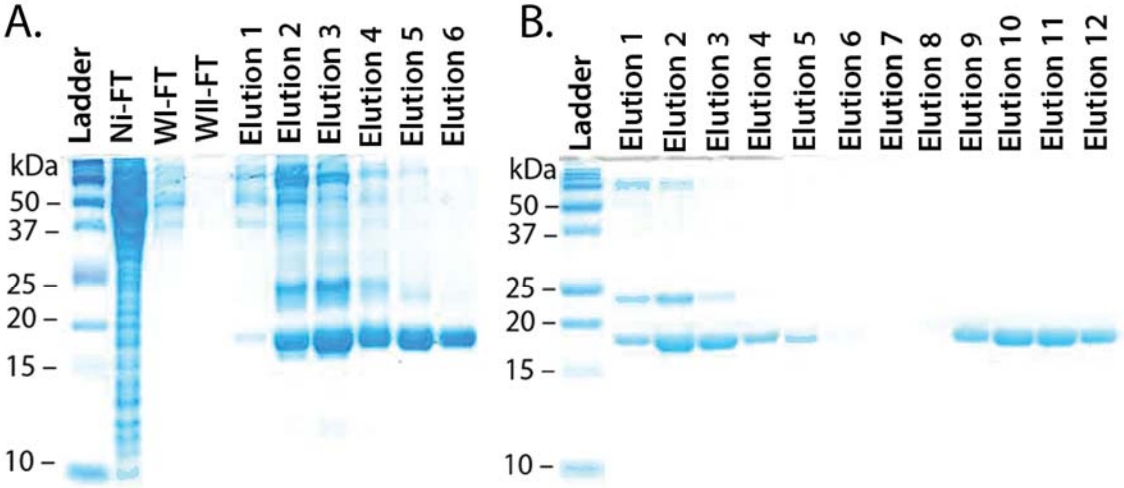

**Figure 4.4. SDS-PAGE of M1 purification optimization.** (A) Stepwise elutions from nickel affinity column show significant large molecular weight impurities (>20 kDa) with the majority of M1 protein (~18 kDa). (B) Elution using an imidazole gradient (50 mM to 300 mM) produced fewer impure fractions and led to the recovery of the bulk of M1 protein in pure elutions. Empty Elutions 6-8 are imidazole transition from 150 to 300 mM.

# Chapter 5 : EPR Spectroscopy of Membrane-Bound M2 in the Presence of M1 Protein

## *5.1. Introduction*

The Howard lab has previously collected continuous wave (CW) and power saturation EPR data for A/Udorn/M2 sites 50-70 in a 4:1 POPC:POPG liposome system and found that M2 is capable of accessing multiple conformational sub-states that are sensitive to changes in the bilayer.[20] We hypothesized that M1 might stabilize one of those conformational sub-states. For our first probe into the interaction of M1 with M2, we selected three M2 protein sites for investigation: residue L43 at the end of the transmembrane region, residue H57 in the C-terminal domain amphipathic helix, and V68 in the distal C-terminal tail before the putative M1 binding site (residues 71-77) (Fig. 5.1A).[35] As can be seen in Figure 5.1B, the residues chosen for labeling are not well conserved, hopefully minimizing perturbations that might occur upon the insertion of a spin label.[67] Previous data from our lab illustrates that sites L43 and H57 produce multicomponent line shapes, corresponding to distinct conformations of the M2 protein, and could potentially function as indicators for shifts in the M2 protein's conformational dynamics. Figure 5.1C highlights the mobile and immobile components of the line shape of sites L43 and H57 and shows the change in conformational equilibria upon addition of cholesterol.[17,20,47]

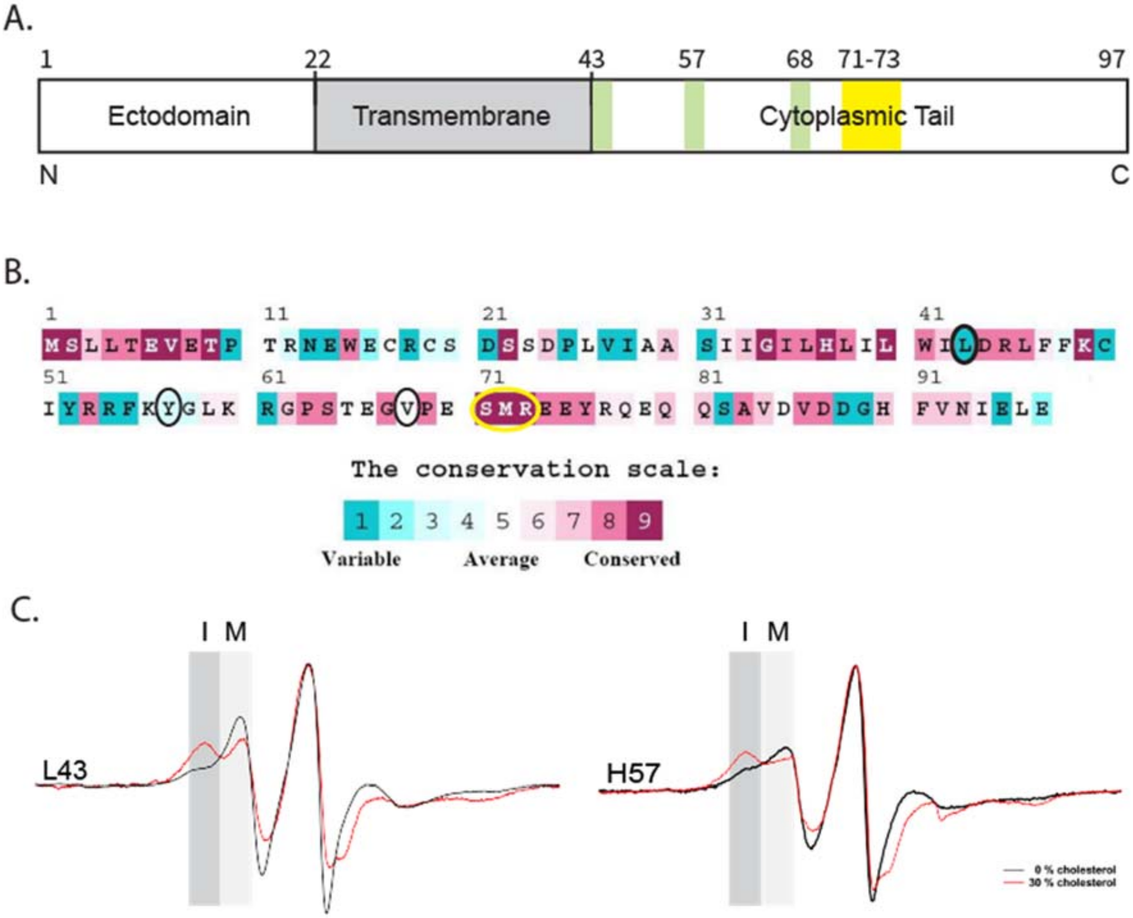

**Figure 5.1. Selection of M2 sites L43, H57, and V68.** (A) Domain map of the M2 protein showing residues selected for investigation (green) and putative M1 binding site (yellow). (B) Heat map of M2 sequence conservation showing selected sites are not well-conserved (circled in black) and putative M1 binding site is generally well-conserved (circled in yellow). Adapted from[67] (C) Previous Howard lab data showing continuous wave EPR spectra for sites L43 and H57 with and without cholesterol in 4:1 POPC:POPG bilayers. Sites L43 and H57 produce spectra with immobile (I) and mobile (M) components. The equilibria between these two states is shifted dramatically with the addition of 30% cholesterol. Adapted from[47]

To interrogate M1-M2 interaction at an atomic level, we used SDSL-EPR spectroscopy to procure EPR line shapes and oxygen power saturation data for the three sites (43, 57, and 68) in membrane reconstituted M2 protein in the presence and absence of the M1 protein. We hypothesized that the M1 protein would interact with the M2 homotetramer shifting M2’s conformational equilibria and oxygen accessibility profile.

### *5.2. Preparation of M2 Proteoliposomes with M1*

The preparation of M2 proteoliposomes is as described in Chapter 3 and the preparation of the M1 protein is as described in Chapter 4.

Flash-frozen M1 aliquots for experimentation were thawed, diluted two-fold, and spun down to remove large aggregates. M2 proteoliposome pellets were resuspended in Extruder Buffer (50 mM Tris pH 8, 100 mM KCl, 1 mM EDTA). Samples with M1 protein were prepared at a 4:1 M2:M1 ratio, reflective of M1 protein interacting with an M2 homotetramer. M1 protein solution was added to resuspended M2 proteoliposomes and the solution was diluted to a final volume three times that of the M1 protein solution added. The resultant sample was nutated overnight for approximately 12 hours at 4°C. The sample was then concentrated to a single pellet as described in Chapter 3 and resuspended in 20 µL of supernatant. Approximately 5 µL of each sample was pulled up into a gas-permeable TPX tube.

CW-EPR spectra were acquired on an X-band Bruker EMX spectrometer at room temperature with 2 mW microwave power, 1 G field modulation amplitude at 100 kHz, and 150 G sweep width. Power saturation data was collected under nitrogen gas conditions at eight power levels or under ambient air conditions at 18 power levels. Analysis of power saturation data to extract $\Delta P_{1/2}(O_2)$ parameters is as described previously.[17]

### *5.3. EPR Line Shapes of M2 in the Presence of M1 Show Slight Decrease in Mobility*

The CW-EPR line shape under different conditions provides information about the relative mobility of the R1 side chain. The line shapes of spin labels on sites 43, 57, and 68 were compared with and without M1. The line shapes of site 43 in the presence and absence of M1 show no observable difference and are essentially superimposable (Fig. 5.2A).

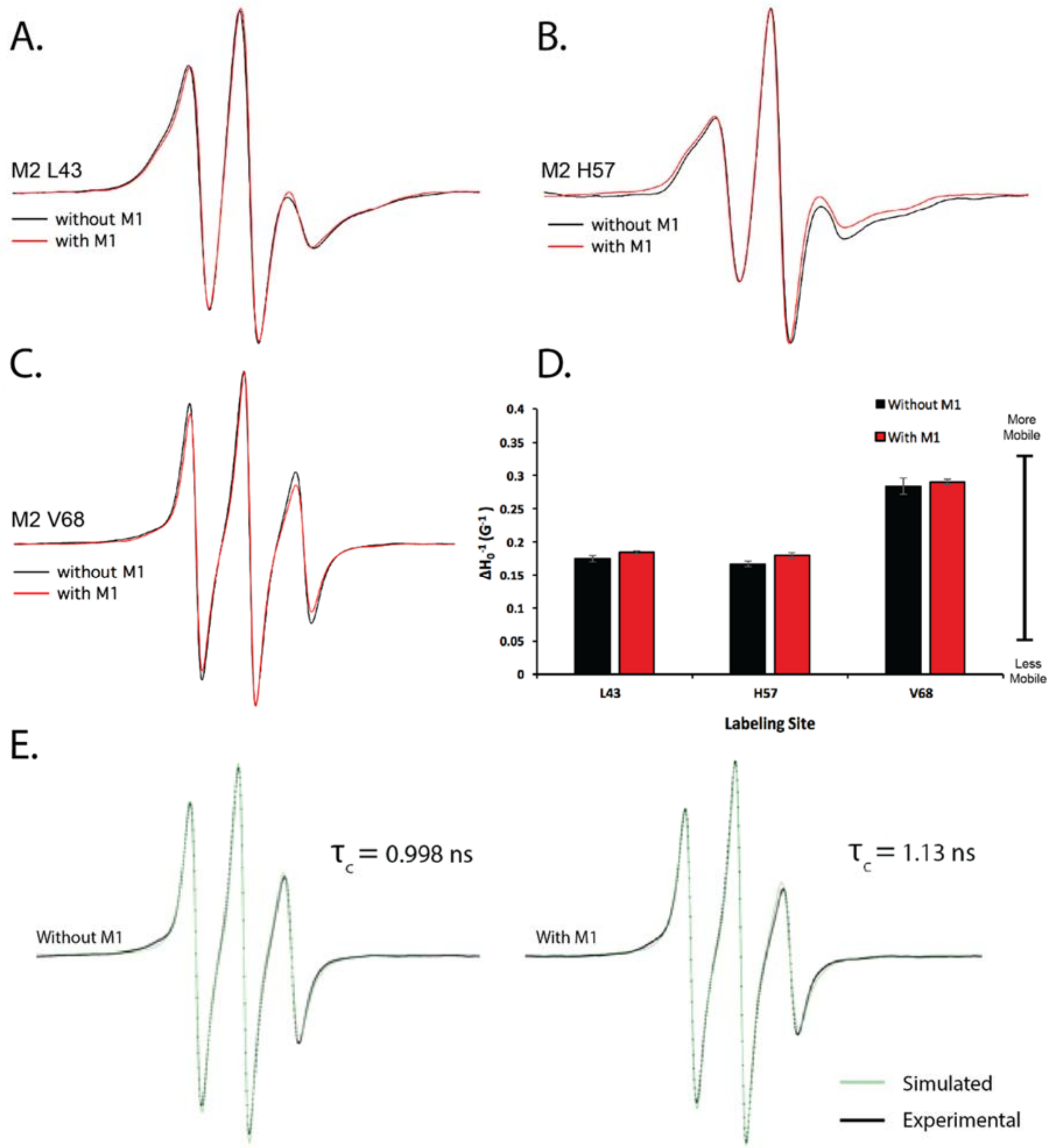

**Figure 5.2**. **CW-EPR line shapes show slight decrease in mobility for M2 sites H57 and V68 in the presence of M1.** M1 conditions correspond to a 4:1 M2:M1 ratio and all M2 constructs were reconstituted in 4:1 POPC:POPG bilayers. Overlay of M2 CW-EPR line shapes for (A) site L43, (B) site H57, and (C) site V68 with (red) and without M1 (black). (D) Inverse central line widths ($\Delta H^{-1}$) for M2 sites L43, H57, and V68. (E) Overlay of actual (black) and simulated (green) spectra for M2 site V68 in the absence (left) and presence (right) of M1 with correlation times ($\tau_c$) extracted from simulated spectra. Correlation times for M2 site V68 are $\tau_c$=0.998 ns without M1 and $\tau_c$=1.13 with M1.

The line shape of site 57 with M1 shows slight broadening compared to line shape without M1 (Fig. 5.2B). The line shape of site 68 with M1 is not entirely superimposable with the line shape of the site without M1 (Fig. 5.2C). The inverse of central line width ($\Delta H^{-1}$), a semi-empirical measure of spectral breadth was calculated for all site CW spectra. This measure of breadth was virtually identical for line shapes with and without M1 (Fig. 5.2D). The single component line shape of site 68 was fit in EasySpin, while the multicomponent line shapes of sites 43 and 57 cannot be fit facilely.[51] Simulation of site 68 line shape without M1 produced a correlation time of 1.00 ns and simulation of line shape with M1 produced a correlation time of 1.13 ns (Fig. 5.2E). Fits were performed by Dr. Kathleen Howard. The increase in correlation time produced by the addition of M1 is indicative of a slight decrease in mobility.

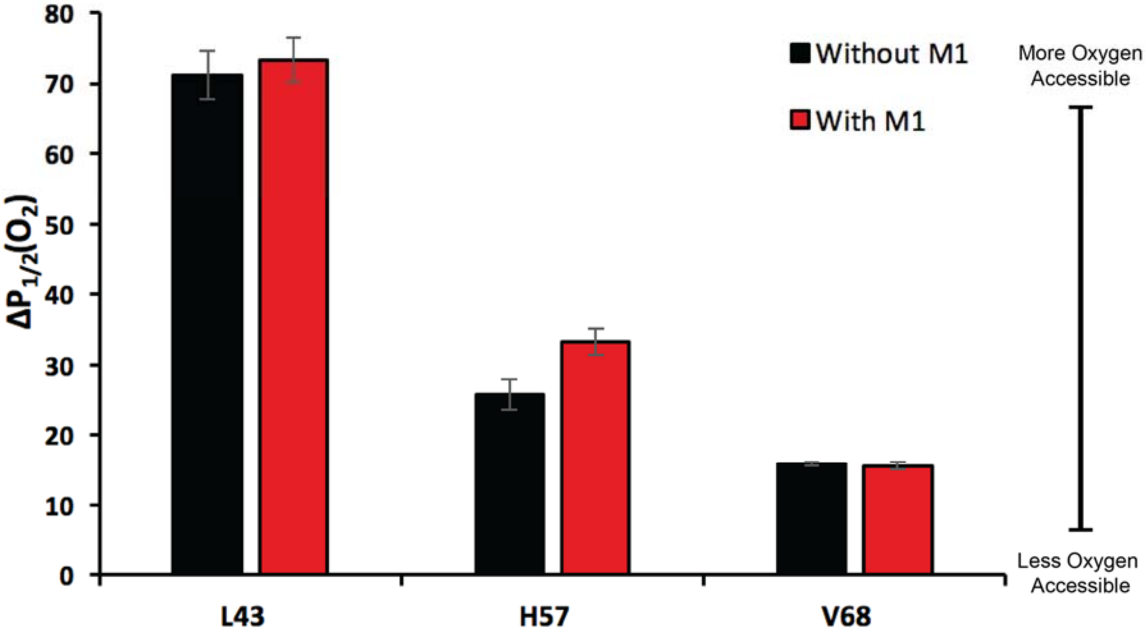

**Figure 5.3. Oxygen accessibility for selected M2 sites show slight increase for M2 site H57 with M1.** M1 conditions correspond to a 4:1 M2:M1 ratio and all M2 constructs were reconstituted in 4:1 POPC:POPG bilayers. Oxygen accessibility parameter, $\Delta P_{1/2}(O_2)$, for M2 sites L43, H57, and V68 are reported. Site H57 shows a slight increase in $\Delta P_{1/2}(O_2)$ in the presence of M1.

### *5.4. M2 Site 57 Shows Slight Increase in Oxygen Accessibility*

Oxygen power saturation data for sites 43 and 68 showed no changes in $\Delta P_{1/2}$ values in the presence or absence of M1 protein (Fig. 5.3). The $\Delta P_{1/2}$ values for membrane-bound M2 in the absence of M1 protein for both sites were consistent with previously collected data.[47,68] Site 57 produced a $\Delta P_{1/2}$ of 25.84 ± 2.2 for sample without M1 and a $\Delta P_{1/2}$ of 33.35 ± 1.8 for sample with M1 (Fig. 5.3). The produced difference in $\Delta P_{1/2}$ values was 7.51, outside of the error range of both $\Delta P_{1/2}$ values.

### *5.5. Discussion*

Comparison of EPR line shapes with and without M1 for sites 43 and 57 produced no visible shift in mobile and immobile components, consistent with a lack of change in M2 conformational equilibria in the presence of M1. Only minor perturbations were observed for any of the selected sites in the presence of M1 and only a small increase in spectral breadth was observed for sites 57 and 68, consistent with a slight decrease in mobility.

Oxygen accessibility was similar between sites 43 and 68 with and without M1 and was only marginally different for site 57. This slight increase in oxygen accessibility could potentially be due to increased membrane depth or the creation of a hydrophobic pocket between M1 and M2. However, the very minor change in all sites in the presence of M1 led us to question the binding interaction between M1 and M2 under our sample conditions. The slight or absent differences could be explained by a lack of M1-M2 binding.

# Chapter 6 : Characterization of the Interaction between M1 and Membrane-Bound M2

## *6.1. Introduction*

EPR spectroscopy of membrane-bound M2 showed very minor changes in the presence of M1 protein. Lack of change could be accounted for by insufficient M1-M2 binding. This binding interaction could be investigated via a sedimentation binding assay, to confirm M1-M2 binding under this study's sample conditions. But first, the presence of M1 protein in the samples used for EPR spectroscopy was confirmed via UV-Vis spectroscopy. The absorbance of the supernatant of M1-M2 samples at 280 nm ($A_{280}$) was taken to determine if M1 was present in the pellet used for EPR analysis. Produced $A_{280}$ values showed little to no protein present in the supernatant, consistent with M1 partitioning into the pellet used for EPR analysis. Then, a sedimentation assay was employed to investigate the M1-M2 binding interaction under our sample conditions. Aggregation of M1 could potentially explain the presence of M1 in the M2 proteoliposome pellet without M1-M2 binding. Samples with just M2 proteoliposomes, 1.8 μM M1 protein or 7.3 μM M1 protein with and without M2 proteoliposomes were prepared, centrifuged, and analyzed by SDS-PAGE.

## *6.2. Sample Preparation*

Samples with proteoliposomes were prepared as described in Chapter 5 but were resuspended in a final volume of 200 μL. Samples with only M1 were prepared in a parallel process. All samples were spun down at 90,000 rpm for 1 hour at 4°C in the TLA-100 rotor of an Optima-MAX-TL ultracentrifuge (Beckman-Coulter). The supernatant was pulled off and the pellet was resuspended in 100 μL of Extruder Buffer (50 mM Tris pH 8, 100 mM KCl, 1 mM EDTA). Supernatant and pellet samples were analyzed by SDS-PAGE.

### *6.3. Sedimentation Assay*

SDS-PAGE gel shows bands corresponding to the molecular weight of M2 for all pellet samples containing M2 proteoliposomes (Fig. 6.1). M2 protein bands show significant spreading due to the presence of lipid in the samples. Samples with M1 at 1.8 μM and 7.3 μM and M2 proteoliposomes show bands corresponding M1 in the pellet sample. Corresponding supernatant samples show no bands, consistent with M1 and M2 partitioning into the pellet. However, the conditions with only M1 at high or low concentrations show no protein bands in the supernatant samples and produced no observable pellet to resuspend.

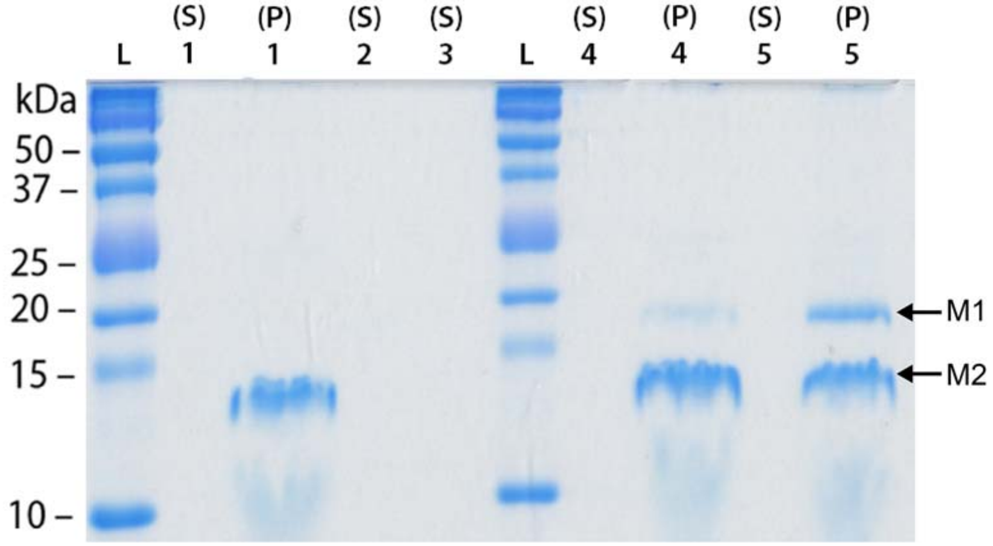

**Figure 6.1. Initial sedimentation assay for M1-M2 binding.** Samples were prepared with 1: only M2 proteoliposomes, 2: only 1.8 μM M1 in solution, 3: only 7.3 μM M1 in solution, 4: 1.8 μM M1 with M2 proteoliposomes, and 5: 7.3 μM M1 with M2 proteoliposomes. Supernatant samples denoted (S) and pellet samples denoted (P). Both M1 and M2 bands appear in the pellet samples for M2 proteoliposomes with low or high M1 concentrations.

*6.4. Discussion*

Both M1 and M2 bands appear in the pellet, but not the supernatant, of samples with M1 and M2 proteoliposomes. This pattern is consistent with M2 pulling M1 down. However, control conditions for M1 in solution showed no observable pellet and no M1 band in the supernatant. This leaves the possibility that M1 formed aggregates and was thus pelleted with M2, so it cannot be concluded that M1 in solution does not pellet out. The lack of a protein band in the supernatant samples of just M1 could be attributed to an extremely low concentration of M1 protein. This low concentration could be the result of aggregate M1 forming a pellet too small to be easily observed, with the amount of remaining soluble M1 too low to be seen on the gel. To more fully elucidate M1-M2 binding, a variation of this sedimentation assay can be repeated.

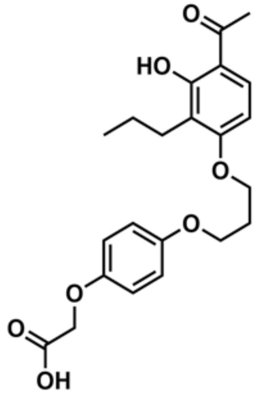

**Figure 6.2. Chemical structure of PHE, a drug that inhibits M1 oligomerization.**

To remove M1 aggregation state as a variable, M1 oligomerization can be mitigated by 4-[3-(4-acetyl-3-hydroxy-2-propylphenoxy)-propoxy]phenoxyacetic acid (PHE), which has been shown to interrupt M1-M1 interactions (Fig. 6.2). PHE was previously identified via virtual screening and found to have an affinity of 50 ± 30 pM for oligomeric M1 and an affinity of 870 ± 150 nM for monomeric M1 at neutral pH. PHE has been shown to be highly potent as a disruptor of M1 oligomerization and is commercially available (Sigma Aldrich CAS 79558-09-1).[27]

# Chapter 7 : Conclusions and Future Directions

## *7.1. Conclusions*

Methods for the overexpression and purification of an N-terminal construct of the M1 protein were developed. Experiments were designed to probe the interaction of M1 and M2. Preliminary biophysical characterization has been carried out using sedimentation and SDSL-EPR of selected M2 sites in the presence of M1.

SDSL-EPR experiments designed to probe the M1-M2 interaction at an atomic level showed little change in the spectra and oxygen accessibility of selected M2 sites (43, 57, 68). Sites 43 and 57 showed little change in their multicomponent spectra, so there seems to be little effect of M1 on M2 conformational equilibria. However, aggregation of M1 could prevent the M1 protein from interacting with enough M2 homotetramers to see a significant change in spectra. This study's chosen stoichiometry of 4:1 M2:M1 may also be insufficient to see a major change in the majority of the M2 population.

Additionally, this study was performed on M2 reconstituted into liposomes, as it is the system in which the Howard lab has previously characterized M2. The directionality of M2 insertion into liposomes under this study's reconstitution conditions is not fully understood and opposing reports exist. Insertion has been reported as both unidirectional and mixed.[69,70] There may not be enough M2 cytoplasmic tails accessible to the M1 protein, due to M2 insertion with the C-terminal region inside the liposome as well as outside of the liposome (Fig. 7.1).

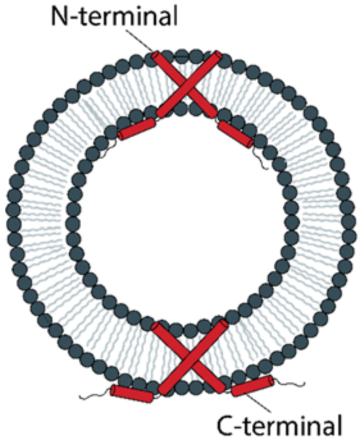

**Figure 7.1. Cartoon of M2 insertion into liposomes.** M2 can insert into liposomes with either the N-terminal or the C-terminal facing outwards.

### *7.2. Future Directions*

There are numerous possible ways to further investigate the interaction between the M1 and M2 proteins. Options for this investigation include controlling the aggregation state of the M1 protein, varying the stoichiometry of M2 and M1, the use of other biophysical techniques, examining the impact of different buffer conditions, using alternate model membrane systems, and different EPR experiments.

#### *7.2.1. Alternate Model Membranes*

Though this study was performed with M2 reconstituted into liposomes, there are a number of other membrane mimetic systems. Lipid nanodiscs or styrene maleic acid co-polymer lipid particles (SMALPS) can also be utilized for the study of the M1-M2 interaction by SDSL-EPR. Lipid nanodiscs consist of a bilayer disk surrounded by a constraining protein, while SMALPS consist of a membrane protein in a bilayer disk that is constrained by styrene maleic acid co-polymer (Fig. 7.2).[71,73,74] In either of these lipid disk systems, all M2 cytoplasmic tails would be accessible to the M1 protein.

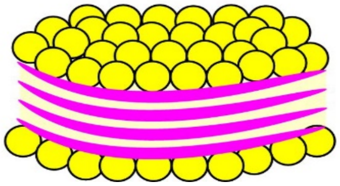

**Figure 7.2. Cartoon of lipid disc model membrane.** From[74]

#### *7.2.2. Aggregation, Stoichiometry, and Sample Conditions*

Assays with the drug PHE, an inhibitor of M1-M1 oligomerization, could help parse out the effect of M1 aggregation on M1-M2 binding. Sedimentation assays and SDSL-EPR experiments in the presence of PHE could be performed to investigate the interaction between the M2 cytoplasmic tail and monomeric M1.

Further SDSL-EPR studies can also vary the M2:M1 ratio to see if there is an increase in spectral change with an increased amount of M1 present. A lower ratio of

M2:M1 could produce a greater change in M2's spectral profile as more individual M2 proteins interact with M1 protein.

Sample buffer conditions could also be varied. Both M2 and M1 are conformationally sensitive to pH. Further studies could make use of a more acidic pH. The salt conditions of the buffer could be altered as well to clarify the nature of the M1-M2 interaction. Raising salt concentration could interrupt electrostatic interactions.

### *7.2.3. Other Biophysical Techniques*

Other biophysical techniques could be used to examine the interaction of the M2 protein with the M1 protein. Dynamic light scattering (DLS) could be performed on M2 proteoliposomes with and without M1, to see if M2 proteoliposomes bind M1 and increase in size. Binding between M1 and M2 could also be pursued using surface plasmon resonance (SPR) or biolayer interferometry (BLI). Recent literature reports binding kinetics studies of membrane proteins by both techniques.[71,72] Molecular docking could also shed light on a potential model for the interaction between the M1 and M2 proteins.

### *7.2.4. Further EPR Experimentation*

Once the M1-M2-membrane system has been more well-established, additional sites along M2's cytoplasmic tail can be investigated by SDSL-EPR. One proposed future site is residue 82 which is after the putative M1 binding site and is not well conserved. A spin label can also be introduced onto a site in the M1 protein, which could potentially be used to acquire distances between a site on the M1 protein and the M2 protein. Expansion of the study could also eventually include the utilization of the full-length M1 protein and M1-vRNP complexes to more accurately represent the *in vivo* interaction of the M1 and M2 proteins.

# Acknowledgements

This project would not have been possible without my partner in lab, Reham Mahgoub ’20, whose help was absolutely invaluable through the ups and downs of this project. I wish her the best of luck on her future projects! I am also incredibly grateful to Alice Herneisen ’17 who mentored me through the beginning of my time in lab and whose name can be found on almost any protocol in the Howard lab. I also want to thank former Howard lab member Hayley Raymond ’18 for being my partner in data collection and endless M2 purifications. I would like to wish Elizabeth Erler ’20 and Dong Ok Kim ’21 a bright future in all their undertakings in the Howard lab.

I also have to thank Laela Ezra ’19, whose support and validation made this project (and my figures) possible. She helped me get the most out of Word and is an all-around excellent person.

Finally, I would like to thank Kathleen Howard for her endless support and patience throughout my two years in lab. She has been the best possible research advisor that I could have asked for.

# References

(1) Panno, J. *Viruses: The Origin and Evolution of Deadly Pathogens*; The new biology: New York, 2011.

(2) Halford, B. Outsmarting Influenza. *C&EN* **2018**, *96* (11), 42–47.

(3) McNeil, D. J. This Flu Season Is the Worst in Nearly a Decade. *The New York Times*. January 26, 2018.

(4) Influenza Antiviral Medications: Summary for Clinicians https://www.cdc.gov/flu/professionals/antivirals/summary-clinicians.htm (accessed Apr 2, 2018).

(5) Das, K.; Aramini, J. M.; Ma, L.-C.; Krug, R. M.; Arnold, E. Structures of Influenza A Proteins and Insights into Antiviral Drug Targets. *Nature Structural & Molecular Biology* **2010**, *17* (5), 530–538. https://doi.org/10.1038/nsmb.1779.

(6) Shi, Y.; Wu, Y.; Zhang, W.; Qi, J.; Gao, G. F. Enabling the "Host Jump": Structural Determinants of Receptor-Binding Specificity in Influenza A Viruses. *Nature Reviews Microbiology* **2014**, *12* (12), 822–831. https://doi.org/10.1038/nrmicro3362.

(7) Samji, T. Influenza A: Understanding the Viral Life Cycle. *Yale J Biol Med* **2009**, *82* (4), 153–159.

(8) Rossman, J. S.; Jing, X.; Leser, G. P.; Lamb, R. A. Influenza Virus M2 Protein Mediates ESCRT-Independent Membrane Scission. *Cell* **2010**, *142* (6), 902–913. https://doi.org/10.1016/j.cell.2010.08.029.

(9) Martyna, A.; Bahsoun, B.; Badham, M. D.; Srinivasan, S.; Howard, M. J.; Rossman, J. S. Membrane Remodeling by the M2 Amphipathic Helix Drives Influenza Virus Membrane Scission. *Scientific Reports* **2017**, *7*, 44695. https://doi.org/10.1038/srep44695.

(10) Rossman, J. S.; Lamb, R. A. Influenza Virus Assembly and Budding. *Virology* **2011**, *411* (2), 229–236. https://doi.org/10.1016/j.virol.2010.12.003.

(11) Chlanda, P.; Zimmerberg, J. Protein-Lipid Interactions Critical to Replication of the Influenza A Virus. *FEBS Lett.* **2016**, *590* (13), 1940–1954. https://doi.org/10.1002/1873-3468.12118.

(12) Sharma, M.; Yi, M.; Dong, H.; Qin, H.; Peterson, E.; Busath, D. D.; Zhou, H.-X.; Cross, T. A. Insight into the Mechanism of the Influenza A Proton Channel from a Structure in a Lipid Bilayer. *Science* **2010**, *330* (6003), 509–512. https://doi.org/10.1126/science.1191750.

(13) Schnell, J. R.; Chou, J. J. Structure and Mechanism of the M2 Proton Channel of Influenza A Virus. *Nature* **2008**, *451* (7178), 591–595. https://doi.org/10.1038/nature06531.

(14) Stouffer, A. L.; Acharya, R.; Salom, D.; Levine, A. S.; Di Costanzo, L.; Soto, C. S.; Tereshko, V.; Nanda, V.; Stayrook, S.; DeGrado, W. F. Structural Basis for the Function and Inhibition of an Influenza Virus Proton Channel. *Nature* **2008**, *451* (7178), 596–599. https://doi.org/10.1038/nature06528.

(15) Cady, S. D.; Schmidt-Rohr, K.; Wang, J.; Soto, C. S.; DeGrado, W. F.; Hong, M. Structure of the Amantadine Binding Site of Influenza M2 Proton Channels in Lipid Bilayers. *Nature* **2010**, *463* (7281), 689–692. https://doi.org/10.1038/nature08722.

(16) Acharya, R.; Carnevale, V.; Fiorin, G.; Levine, B. G.; Polishchuk, A. L.; Balannik, V.; Samish, I.; Lamb, R. A.; Pinto, L. H.; DeGrado, W. F.; et al. Structure and Mechanism of Proton Transport through the Transmembrane Tetrameric M2 Protein Bundle of the Influenza A Virus. *PNAS* **2010**, *107* (34), 15075–15080. https://doi.org/10.1073/pnas.1007071107.

(17) Nguyen, P. A.; Soto, C. S.; Polishchuk, A.; Caputo, G. A.; Tatko, C. D.; Ma, C.; Ohigashi, Y.; Pinto, L. H.; DeGrado, W. F.; Howard, K. P. PH-Induced Conformational Change of the Influenza M2 Protein C-Terminal Domain. *Biochemistry* **2008**, *47* (38), 9934–9936. https://doi.org/10.1021/bi801315m.

(18) Fiorin, G.; Carnevale, V.; DeGrado, W. F. The Flu's Proton Escort. *Science* **2010**, *330* (6003), 456–458. https://doi.org/10.1126/science.1197748.

(19) Iwatsuki-Horimoto, K.; Horimoto, T.; Noda, T.; Kiso, M.; Maeda, J.; Watanabe, S.; Muramoto, Y.; Fujii, K.; Kawaoka, Y. The Cytoplasmic Tail of the Influenza A Virus M2 Protein Plays a Role in Viral Assembly. *Journal of Virology* **2006**, *80* (11), 5233–5240. https://doi.org/10.1128/JVI.00049-06.

(20) Kim, S. S.; Upshur, M. A.; Saotome, K.; Sahu, I. D.; McCarrick, R. M.; Feix, J. B.; Lorigan, G. A.; Howard, K. P. Cholesterol-Dependent Conformational Exchange of the C-Terminal Domain of the Influenza A M2 Protein. *Biochemistry* **2015**, *54* (49), 7157–7167. https://doi.org/10.1021/acs.biochem.5b01065.

(21) Huang, S.; Green, B.; Thompson, M.; Chen, R.; Thomaston, J.; DeGrado, W. F.; Howard, K. P. C-Terminal Juxtamembrane Region of Full-Length M2 Protein Forms a Membrane Surface Associated Amphipathic Helix. *Protein Sci* **2015**, *24* (3), 426–429. https://doi.org/10.1002/pro.2631.

(22) Kim, G.; Raymond, H. E.; Herneisen, A. L.; Wong-Rolle, A. J.; Howard, K. P. The Distal Cytoplasmic Tail of the Influenza A M2 Protein Dynamically Extends from the Membrane. *BBA Biomembranes* **in press**.

(23) Safo, M. K.; Musayev, F. N.; Mosier, P. D.; Zhou, Q.; Xie, H.; Desai, U. R. Crystal Structures of Influenza A Virus Matrix Protein M1: Variations on a Theme. *PLoS ONE* **2014**, *9* (10), e109510. https://doi.org/10.1371/journal.pone.0109510.

(24) Arzt, S.; Baudin, F.; Barge, A.; Timmins, P.; Burmeister, W. P.; Ruigrok, R. W. H. Combined Results from Solution Studies on Intact Influenza Virus M1 Protein and from a New Crystal Form of Its N-Terminal Domain Show That M1 Is an Elongated Monomer. *Virology* **2001**, *279* (2), 439–446. https://doi.org/10.1006/viro.2000.0727.

(25) Harris, A.; Forouhar, F.; Qiu, S.; Sha, B.; Luo, M. The Crystal Structure of the Influenza Matrix Protein M1 at Neutral PH: M1–M1 Protein Interfaces Can Rotate in the Oligomeric Structures of M1. *Virology* **2001**, *289* (1), 34–44. https://doi.org/10.1006/viro.2001.1119.

(26) Sha, B.; Luo, M. Structure of a Bifunctional Membrane-RNA Binding Protein, Influenza Virus Matrix Protein M1. *Nature Structural & Molecular Biology* **1997**, *4* (3), 239–244. https://doi.org/10.1038/nsb0397-239.

(27) Mosier, P. D.; Chiang, M.-J.; Lin, Z.; Gao, Y.; Althufairi, B.; Zhou, Q.; Musayev, F.; Safo, M. K.; Xie, H.; Desai, U. R. Broad Spectrum Anti-Influenza Agents by Inhibiting Self-Association of Matrix Protein 1. *Scientific Reports* **2016**, *6* (1). https://doi.org/10.1038/srep32340.

(28) Shtykova, E. V.; Dadinova, L. A.; Fedorova, N. V.; Golanikov, A. E.; Bogacheva, E. N.; Ksenofontov, A. L.; Baratova, L. A.; Shilova, L. A.; Tashkin, V. Y.; Galimzyanov, T. R.; et al. Influenza Virus Matrix Protein M1 Preserves Its Conformation with PH, Changing Multimerization State at the Priming Stage Due to Electrostatics. *Scientific Reports* **2017**, *7* (1), 16793. https://doi.org/10.1038/s41598-017-16986-y.

(29) Liu, H.; Grantham, M. L.; Pekosz, A. Mutations in the Influenza A Virus M1 Protein Enhance Virus Budding To Complement Lethal Mutations in the M2 Cytoplasmic Tail. *Journal of Virology* **2018**, *92* (1), e00858-17. https://doi.org/10.1128/JVI.00858-17.

(30) Roberts, P. C.; Lamb, R. A.; Compans, R. W. The M1 and M2 Proteins of Influenza A Virus Are Important Determinants in Filamentous Particle Formation. *Virology* **1998**, *240* (1), 127–137. https://doi.org/10.1006/viro.1997.8916.

(31) Elleman, C. J.; Barclay, W. S. The M1 Matrix Protein Controls the Filamentous Phenotype of Influenza A Virus. *Virology* **2004**, *321* (1), 144–153. https://doi.org/10.1016/j.virol.2003.12.009.

(32) Rossman, J. S.; Jing, X.; Leser, G. P.; Balannik, V.; Pinto, L. H.; Lamb, R. A. Influenza Virus M2 Ion Channel Protein Is Necessary for Filamentous Virion Formation. *Journal of Virology* **2010**, *84* (10), 5078–5088. https://doi.org/10.1128/JVI.00119-10.

(33) Chen, B. J.; Leser, G. P.; Morita, E.; Lamb, R. A. Influenza Virus Hemagglutinin and Neuraminidase, but Not the Matrix Protein, Are Required for Assembly and Budding of Plasmid-Derived Virus-Like Particles. *Journal of Virology* **2007**, *81* (13), 7111–7123. https://doi.org/10.1128/JVI.00361-07.

(34) McCown, M. F.; Pekosz, A. The Influenza A Virus M2 Cytoplasmic Tail Is Required for Infectious Virus Production and Efficient Genome Packaging. *J Virol* **2005**, *79* (6), 3595–3605. https://doi.org/10.1128/JVI.79.6.3595-3605.2005.

(35) McCown, M. F.; Pekosz, A. Distinct Domains of the Influenza A Virus M2 Protein Cytoplasmic Tail Mediate Binding to the M1 Protein and Facilitate Infectious Virus Production. *J. Virol.* **2006**, *80* (16), 8178–8189. https://doi.org/10.1128/JVI.00627-06.

(36) Zebedee, S. L.; Lamb, R. A. Growth Restriction of Influenza A Virus by M2 Protein Antibody Is Genetically Linked to the M1 Protein. *Proc Natl Acad Sci U S A* **1989**, *86* (3), 1061–1065.

(37) Wang, D.; Harmon, A.; Jin, J.; Francis, D. H.; Christopher-Hennings, J.; Nelson, E.; Montelaro, R. C.; Li, F. The Lack of an Inherent Membrane Targeting Signal Is Responsible for the Failure of the Matrix (M1) Protein of Influenza A Virus to Bud into Virus-like Particles. *J. Virol.* **2010**, *84* (9), 4673–4681. https://doi.org/10.1128/JVI.02306-09.

(38) Chen, B. J.; Leser, G. P.; Jackson, D.; Lamb, R. A. The Influenza Virus M2 Protein Cytoplasmic Tail Interacts with the M1 Protein and Influences Virus Assembly at the Site of Virus Budding. *J Virol* **2008**, *82* (20), 10059–10070. https://doi.org/10.1128/JVI.01184-08.

(39) Carpenter, E. P.; Beis, K.; Cameron, A. D.; Iwata, S. Overcoming the Challenges of Membrane Protein Crystallography. *Curr Opin Struct Biol* **2008**, *18* (5), 581–586. https://doi.org/10.1016/j.sbi.2008.07.001.

(40) Sahu, I. D.; McCarrick, R. M.; Lorigan, G. A. Use of Electron Paramagnetic Resonance To Solve Biochemical Problems. *Biochemistry* **2013**, *52* (35), 5967–5984. https://doi.org/10.1021/bi400834a.

(41) Weil, J. A.; Bolton, J. R.; Wertz, J. E. *Electron Paramagnetic Resonance: Elementary Theory and Practical Applications*; John Wiley & Sons: New York, 1994.

(42) Weber, R. T. *Xenon User's Guide*; Bruker BioSpin Corporation.

(43) Bordignon, E. Site-Directed Spin Labeling of Membrane Proteins. In *EPR Spectroscopy*; Drescher, M., Jeschke, G., Eds.; Springer Berlin Heidelberg: Berlin, Heidelberg, 2011; Vol. 321, pp 121–157. https://doi.org/10.1007/128_2011_243.

(44) Altenbach, C.; López, C. J.; Hideg, K.; Hubbell, W. L. Exploring Structure, Dynamics, and Topology of Nitroxide Spin-Labeled Proteins Using Continuous-Wave Electron Paramagnetic Resonance Spectroscopy. In *Methods in Enzymology*; Qin, P. Z., Warncke, K., Eds.; Electron Paramagnetic Resonance Investigations of Biological Systems by Using Spin Labels, Spin Probes, and Intrinsic Metal Ions, Part B; Academic Press, 2015; Vol. 564, pp 59–100. https://doi.org/10.1016/bs.mie.2015.08.006.

(45) Sahu, I. D.; Lorigan, G. A. Site-Directed Spin Labeling EPR for Studying Membrane Proteins. *Biomed Res Int* **2018**, *2018*. https://doi.org/10.1155/2018/3248289.

(46) Berliner, L. J. *Spin Labeling: Theory and Applications*; Molecular Biology: An International Series of Monographs and Textbooks; Academic Press: New York, 1976.

(47) Herneisen, A. L. Conformational Studies of a Domain of the Influenza A M2 Protein Involved in Viral Budding and Morphology, Swarthmore College, 2017.

(48) Fleissner, M. R.; Bridges, M. D.; Brooks, E. K.; Cascio, D.; Kálai, T.; Hideg, K.; Hubbell, W. L. Structure and Dynamics of a Conformationally Constrained Nitroxide Side Chain and Applications in EPR Spectroscopy. *Proc Natl Acad Sci U S A* **2011**, *108* (39), 16241–16246. https://doi.org/10.1073/pnas.1111420108.

(49) Hubbell, W. L.; Mchaourab, H. S.; Altenbach, C.; Lietzow, M. A. Watching Proteins Move Using Site-Directed Spin Labeling. *Structure* **1996**, *4* (7), 779–783. https://doi.org/10.1016/S0969-2126(96)00085-8.

(50) Klare, J. P.; Steinhoff, H.-J. Spin Labeling EPR. *Photosynthesis Research* **2009**, *102* (2–3), 377–390. https://doi.org/10.1007/s11120-009-9490-7.

(51) Stoll, S.; Schweiger, A. EASYSPIN: SIMULATING CW ESR SPECTRA. 24.

(52) Guzzi, R.; Bartucci, R. Electron Spin Resonance of Spin-Labeled Lipid Assemblies and Proteins. *Archives of Biochemistry and Biophysics* **2015**, *580*, 102–111. https://doi.org/10.1016/j.abb.2015.06.015.

(53) Klug, C. S.; Feix, J. B. Methods and Applications of Site-Directed Spin Labeling EPR Spectroscopy. In *Methods in Cell Biology*; Biophysical Tools for Biologists, Volume One: In Vitro Techniques; Academic Press, 2008; Vol. 84, pp 617–658. https://doi.org/10.1016/S0091-679X(07)84020-9.

(54) Altenbach, C.; Froncisz, W.; Hemker, R.; Mchaourab, H.; Hubbell, W. L. Accessibility of Nitroxide Side Chains: Absolute Heisenberg Exchange Rates from Power Saturation EPR. *Biophysical Journal* **2005**, *89* (3), 2103–2112. https://doi.org/10.1529/biophysj.105.059063.

(55) Jungnick, N. Influenza Matrix Protein M1 – An in Vitro Membrane Binding Study, Humboldt-Universität zu Berlin, 2011.

(56) Martínez-Alonso, M.; González-Montalbán, N.; García-Fruitós, E.; Villaverde, A. Learning about Protein Solubility from Bacterial Inclusion Bodies. *Microb Cell Fact* **2009**, *8*, 4. https://doi.org/10.1186/1475-2859-8-4.

(57) Singh, A.; Upadhyay, V.; Upadhyay, A. K.; Singh, S. M.; Panda, A. K. Protein Recovery from Inclusion Bodies of Escherichia Coli Using Mild Solubilization Process. *Microbial Cell Factories* **2015**, *14*, 41. https://doi.org/10.1186/s12934-015-0222-8.

(58) Thomson, C. A.; Olson, M.; Jackson, L. M.; Schrader, J. W. A Simplified Method for the Efficient Refolding and Purification of Recombinant Human GM-CSF. *PLOS ONE* **2012**, *7* (11), e49891. https://doi.org/10.1371/journal.pone.0049891.

(59) *The QIAexpressionist*, 5th ed.; QIAGEN Worldwide.

(60) Upadhyay, A. K.; Singh, A.; Mukherjee, K. J.; Panda, A. K. Refolding and Purification of Recombinant L-Asparaginase from Inclusion Bodies of E. Coli into Active Tetrameric Protein. *Front. Microbiol.* **2014**, *5*. https://doi.org/10.3389/fmicb.2014.00486.

(61) Burgess, R. R. Purification of Overproduced Escherichia Coli RNA Polymerase Sigma Factors by Solubilizing Inclusion Bodies and Refolding from Sarkosyl. *Meth. Enzymol.* **1996**, *273*, 145–149.

(62) Palmer, I.; Wingfield, P. T. Preparation and Extraction of Insoluble (Inclusion-Body) Proteins from Escherichia Coli. *Curr Protoc Protein Sci* **2004**, *CHAPTER*, Unit-6.3. https://doi.org/10.1002/0471140864.ps0603s38.

(63) Oganesyan, N.; Kim, S.-H.; Kim, R. On-Column Protein Refolding for Crystallization. *J. Struct. Funct. Genomics* **2005**, *6* (2–3), 177–182. https://doi.org/10.1007/s10969-005-2827-3.

(64) Veldkamp, C. T.; Peterson, F. C.; Hayes, P. L.; Mattmiller, J. E.; Haugner, J. C.; de la Cruz, N.; Volkman, B. F. On-Column Refolding of Recombinant Chemokines for NMR Studies and Biological Assays. *Protein Expr. Purif.* **2007**, *52* (1), 202–209. https://doi.org/10.1016/j.pep.2006.09.009.

(65) Jungbauer, A.; Kaar, W. Current Status of Technical Protein Refolding. *Journal of Biotechnology* **2007**, *128* (3), 587–596. https://doi.org/10.1016/j.jbiotec.2006.12.004.

(66) Singh, S. M.; Panda, A. K. Solubilization and Refolding of Bacterial Inclusion Body Proteins. *Journal of Bioscience and Bioengineering* **2005**, *99* (4), 303–310. https://doi.org/10.1263/jbb.99.303.

(67) Darapaneni, V. Large-Scale Analysis of Influenza A Virus Sequences Reveals Universally Conserved Residues of Matrix Proteins. **2015**, *3* (1), 13.

(68) Kim, G. SDSL-EPR of Residues 60-70 of Influenza M2 Protein Reveals Structural Properties of a Region Involved in Viral Budding, Swarthmore College, 2017.

(69) Raymond, H. E. Conformation and Directionality of the Influenza A M2 Protein Domain Essential to Viral Replication, Swarthmore College, 2018.

(70) Leiding, T. Probing Proton Translocation in Influenza A/M2 Proteoliposomes, Lund University, 2010.

(71) Rouck, J.; Krapf, J.; Roy, J.; Huff, H.; Das, A. Recent Advances in Nanodisc Technology for Membrane Proteins Studies (2012–2017). *FEBS Lett* **2017**, *591* (14), 2057–2088. https://doi.org/10.1002/1873-3468.12706.

(72) Sharma, S.; Wilkens, S. Biolayer Interferometry of Lipid Nanodisc-reconstituted Yeast Vacuolar H+-ATPase. *Protein Sci* **2017**, *26* (5), 1070–1079. https://doi.org/10.1002/pro.3143.

(73) Parmar, M. J.; Lousa, C. D. M.; Muench, S. P.; Goldman, A.; Postis, V. L. G. Artificial Membranes for Membrane Protein Purification, Functionality and Structure Studies. *Biochemical Society Transactions* **2016**, *44* (3), 877–882. https://doi.org/10.1042/BST20160054.

(74) Postis, V.; Rawson, S.; Mitchell, J. K.; Lee, S. C.; Parslow, R. A.; Dafforn, T. R.; Baldwin, S. A.; Muench, S. P. The Use of SMALPs as a Novel Membrane Protein Scaffold for Structure Study by Negative Stain Electron Microscopy. *Biochimica et Biophysica Acta (BBA) - Biomembranes* **2015**, *1848* (2), 496–501. https://doi.org/10.1016/j.bbamem.2014.10.018.